

Theoretical modeling of capillary surfer interactions on a vibrating fluid bathAnand U. Oza ^{1,*}, Giuseppe Pucci ^{2,3}, Ian Ho,⁴ and Daniel M. Harris ⁴¹*Department of Mathematical Sciences & Center for Applied Mathematics and Statistics,
New Jersey Institute of Technology, Newark, New Jersey 07102, USA*²*Consiglio Nazionale delle Ricerche–Istituto di Nanotecnologia (CNR-NANOTEC),
Via P. Bucci 33C, 87036 Rende, Italy*³*INFN, Sezione di Lecce, Via per Monteroni, Lecce 73100, Italy*⁴*School of Engineering, Brown University, 184 Hope Street, Providence, Rhode Island 02912, USA*

(Received 13 January 2023; accepted 26 September 2023; published 7 November 2023)

We present and analyze a theoretical model for the dynamics and interactions of “capillary surfers,” which are millimetric objects that self-propel while floating at the interface of a vibrating fluid bath. In our companion paper [I. Ho *et al.*, [Phys. Rev. Fluids](#) **8**, L112001 (2023)], we reported the results of an experimental investigation of the surfer system, which showed that surfer pairs may lock into one of seven bound states, and that larger collectives of surfers self-organize into coherent flocking states. Our theoretical model for the surfers’ positional and orientational dynamics approximates a surfer as a pair of vertically oscillating point sources of weakly viscous gravity-capillary waves. We derive an analytical solution for the associated interfacial deformation and thus the hydrodynamic force exerted by one surfer on another. Our model recovers the bound states found in experiments and exhibits good agreement with experimental data. Moreover, we conduct a linear stability analysis of bound state solutions and compute numerically the associated eigenvalues. We find that the spacings of the bound states are quantized on the capillary wavelength, with stable branches of equilibria separated by unstable ones. Generally, our work shows that self-propelling objects coupled by capillary waves constitute a promising platform for studying active matter systems in which both inertial and viscous effects are relevant.

DOI: [10.1103/PhysRevFluids.8.114001](https://doi.org/10.1103/PhysRevFluids.8.114001)**I. INTRODUCTION**

Over the last several decades, there has been significant interest in understanding the physics of so-called “wet” active matter systems, in which constituents consume energy in order to move through a fluid medium [1–3]. Such systems are ubiquitous in biology and span the Reynolds-number spectrum. On one end, organisms at the microscale interact through low-Reynolds number (viscous or Stokesian) hydrodynamic interactions [4–6]. On the other end, schools of fish and flocks of birds generate relatively high-Reynolds number flows in which inertial effects are dominant [7–9]. Interfacial active systems consist of objects or organisms that self-propel at a liquid-gas interface and typically exist in an intermediate regime in which both inertial and viscous forces are relevant [10]. Examples include water-walking insects [11–14], bio-inspired self-propellers [15], and self-assembled magnetic swimmers [16–19]. Prior work has shown that floating solid bodies can self-propel due to the net flow generated by AC electrowetting [20], and that floating water droplets [21–23] and bouncing oil droplets [24,25] may self-propel across a vibrating fluid bath

*oza@njit.edu

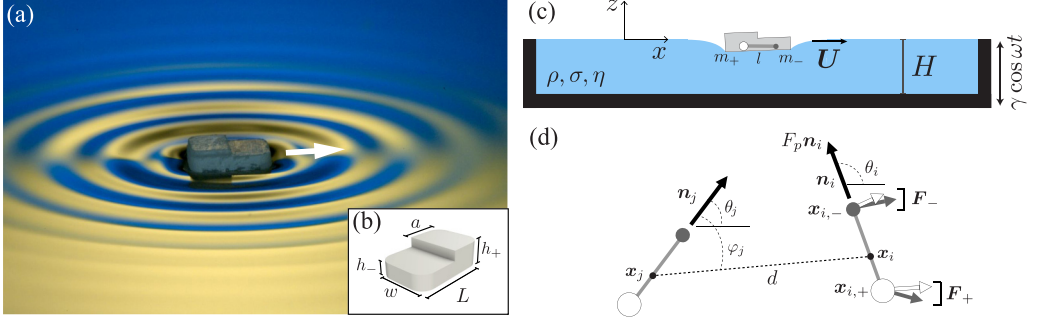


FIG. 1. A capillary surfer self-propels on a fluid interface due to its self-generated waves. (a) Oblique wave field visualization, in which colors are obtained from the distorted reflection of a yellow and blue background on the fluid surface. (b) Surfer geometry used in experiments. (c) Side view schematic of the experimental setup (not to scale). The fluid has density ρ , surface tension σ , dynamic viscosity η , and depth H . The theoretical idealization of the surfer is superposed: the surfer is represented as two unequal masses m_+ and m_- connected by a rod of length l . (d) Top view schematics of the theoretical model: a surfer with center-of-mass \mathbf{x}_i experiences a propulsive force $F_p \mathbf{n}_i$, and its associated masses located at $\mathbf{x}_{i,+}$ (white) and $\mathbf{x}_{i,-}$ (gray) experience capillary forces \mathbf{F}_\pm (thick arrows) due to the masses making up the j th surfer.

due to interfacial Faraday waves. Moreover, camphor boats self-propel due to gradients in surface tension [26,27] and thus exhibit rich collective behavior [28–31].

In a companion paper [32], we report the discovery of an interfacial active system called “capillary surfers” [Fig. 1(a)]. A surfer consists of a millimetric hydrophobic body [Fig. 1(b)] that floats on the surface of a vertically vibrating fluid bath of a water-glycerol mixture [Fig. 1(c)]. All experiments are performed below the Faraday instability threshold, above which subharmonic standing waves spontaneously form at the free surface [33]. A surfer is front-back asymmetric and thus tilts slightly backwards in equilibrium, with the contact line remaining pinned to the surfer’s base perimeter. The vibration of the bath results in the vertical oscillation of the surfer and the subsequent generation of a radiated, propagating wave field. The surfer thus moves along its long axis in the direction of its thinner half [Figs. 1(a) and 1(c)], the velocity being constant in the absence of external perturbations and other surfers. In the following we refer to the front and back of the surfer as the “bow” and “stern,” respectively.

For a given surfer geometry, the surfer speed increases with the forcing acceleration and decreases with the forcing frequency (Fig. S1 in [32]). Moreover, surfers interact through the wave fields that they generate and thus exhibit unique collective behavior. Specifically, experiments have demonstrated that when pairs of surfers are set into motion towards each other, they may spontaneously arrange into a variety of different bound states (Fig. 2 in [32]). The system also exhibits multistability: multiple bound states may coexist for the same experimental parameters, and these states are quantized on the capillary length (Fig. 3 in [32]). Collections of more surfers may self-organize due to their mutual capillary wave field and exhibit ordered flocking states (Fig. 4 in [32]). The goal of this paper is to construct and analyze a theoretical model for capillary surfer interactions in order to rationalize the experimental observations.

In order to build such a model, we require a theory for the interfacial deformation induced by capillary-scale floating objects. Approximate expressions for the capillary forces between stationary spherical and cylindrical bodies have been derived [34–38], and review articles have detailed experimental and theoretical efforts to understand the capillary interactions between bodies trapped at fluid interfaces [39,40]. The *dynamic* problem, wherein the bodies oscillate at the interface and thus generate a time-dependent wave field, has received comparatively less attention. Prior work has focused on the deformations generated by relatively large bodies, for which gravitational forces dominate over surface tension [41]. Asymptotic expressions in both the long- [42] and short-wave

limits [43–48] have been derived. De Corato and Garbin [49] were the first to derive expressions for small-amplitude capillary waves generated by a periodically oscillating point force at the interface and the resulting lateral capillary forces experienced by two oscillating point particles.

The outline of the theoretical model presented in this paper is as follows. We model the dynamics of each surfer’s center of mass and orientation in the plane [Fig. 1(d)], assuming these dynamics to be decoupled from the surfer’s periodic vertical motion. The propulsive force on each surfer is inferred from experimental measurements of the free speed of a single surfer. Since there does not exist an analytical expression for the capillary force between two finite-sized objects oscillating on a fluid interface, we model each surfer as a pair of oscillating masses, chosen to represent the surfer’s asymmetric mass distribution in experiments [Fig. 1(b)]. The surfers interact through the interfacial deformation generated by these masses. The “static” part of the resulting force, due to the surfer’s weight, is approximated by treating each mass as a disk. The “dynamic” part of the force, due to the surfer’s oscillation at the interface, is approximated by treating each mass as a point particle.

To obtain an expression for the dynamic force, in Sec. II we generalize De Corato and Garbin’s work [49] to account for the effects of gravity and weak viscosity. We thus obtain in Sec. III a formula for the combined static and dynamic forces between two bodies that oscillate at a fluid interface. This formula is used in Sec. IV to produce a trajectory equation for capillary surfers that interact through their collectively generated wave field. In Sec. V we examine the existence and stability of bound states of surfer pairs and compare our results with experimental data reported in our companion paper [32]. Examples of collective modes exhibited by larger populations of surfers are given in Sec. VI. Conclusions and avenues for future work are presented in Sec. VII.

II. WEAKLY VISCOUS LINEAR WAVES GENERATED BY AN OSCILLATING POINT FORCE

In this section we derive the linear wave field generated by a point force oscillating harmonically on the free surface of a fluid bath. In the experiments [32], the entire fluid bath is shaken vertically with an acceleration $\gamma \cos(\omega t)$ below the Faraday instability threshold, so we neglect the effects of parametric forcing on the waves. Our analysis generalizes the potential flow model of De Corato and Garbin [49] by accounting for gravity and weak viscosity. The latter is incorporated by using the so-called quasipotential formalism first given by Lamb [50] and then Dias *et al.* [51], wherein viscous corrections to the free surface boundary conditions are derived by assuming that the waves are irrotational and inviscid at leading order, but that dissipation occurs in a viscous boundary layer at the free surface. We adapt the governing equations derived by Milewski *et al.* [52], who generalized the formalism in Ref. [51] to include surface tension. The model in Ref. [52] has been used profitably to simulate the pilot-wave dynamics of liquid droplets bouncing on a liquid bath [53–57], and accurately predicts the time-dependent wave field and trajectories of capillary-scale rebounds of nonwetting particles and droplets [58,59].

Consider an incompressible fluid in an infinite domain (\mathbf{x}, z) , where $\mathbf{x} \in \mathbb{R}^2$ and $z < 0$, $z = 0$ being the mean position of the free surface. The fluid has density ρ , surface tension σ , and kinematic viscosity ν , and evolves under the influence of a gravitational acceleration g and an oscillating point force with amplitude F_0 and frequency ω . The relevant variables and their characteristic values are listed in Table I. Assuming that the waves are of small amplitude so that the governing equations may be linearized, the free surface height $h(\mathbf{x}, t)$ and velocity potential $\phi(\mathbf{x}, z, t)$ satisfy the system

$$\begin{aligned} \Delta \phi + \partial_{zz} \phi &= 0, \quad z < 0, \quad \mathbf{x} \in \mathbb{R}^2, \\ \partial_t \phi &= -gh + \frac{\sigma}{\rho} \Delta h + 2\nu \Delta \phi + \frac{F_0}{\rho} \cos \omega t \delta(\mathbf{x}) \quad \text{at } z = 0, \\ \partial_t h &= \partial_z \phi + 2\nu \Delta h \quad \text{at } z = 0, \\ \phi &\rightarrow 0, \quad h \rightarrow 0 \quad \text{as } |\mathbf{x}|, z \rightarrow \infty, \end{aligned} \tag{1}$$

where $\Delta = \partial_{xx} + \partial_{yy}$. The first equation follows from the assumptions that the fluid is incompressible and irrotational, while the second and third equations are, respectively, the dynamic and kinematic conditions at the free surface.

We solve these equations by writing $\phi(\mathbf{x}, z, t) = \text{Re}[\phi_1(\mathbf{x}, z)e^{i\omega t}]$ and $h(\mathbf{x}, t) = \text{Re}[h_1(\mathbf{x})e^{i\omega t}]$, where

$$\phi_1(\mathbf{x}, z) = \int_{\mathbb{R}^2} \hat{\phi}_1(\mathbf{k}, z)e^{i\mathbf{k}\cdot\mathbf{x}} d\mathbf{k} \quad \text{and} \quad h_1(\mathbf{x}) = \int_{\mathbb{R}^2} \hat{h}_1(\mathbf{k})e^{i\mathbf{k}\cdot\mathbf{x}} d\mathbf{k}. \quad (2)$$

The Fourier-transformed quantities $\hat{\phi}_1$ and \hat{h}_1 satisfy the algebraic equations

$$\begin{aligned} \partial_{zz}\hat{\phi}_1 - |\mathbf{k}|^2\hat{\phi}_1 &= 0, \quad i\omega\hat{\phi}_1(\mathbf{k}, 0) = -g\hat{h}_1 - \frac{\sigma}{\rho}|\mathbf{k}|^2\hat{h}_1 - 2\nu|\mathbf{k}|^2\hat{\phi}_1 + \frac{F_0}{(2\pi)^2\rho}, \\ i\omega\hat{h}_1 &= \partial_z\hat{\phi}_1(\mathbf{k}, 0) - 2\nu|\mathbf{k}|^2\hat{h}_1. \end{aligned} \quad (3)$$

Writing $\hat{\phi}_1(\mathbf{k}, z) = A(\mathbf{k})e^{k|z|}$, we obtain expressions for \hat{h}_1 and A :

$$\begin{aligned} \hat{h}_1(\mathbf{k}) &= \frac{F_0}{(2\pi)^2} \frac{|\mathbf{k}|}{\rho(i\omega + 2\nu|\mathbf{k}|^2)^2 + (\rho g + \sigma|\mathbf{k}|^2)|\mathbf{k}|} \quad \text{and} \\ A(\mathbf{k}) &= \frac{F_0}{(2\pi)^2} \frac{i\omega + 2\nu|\mathbf{k}|^2}{\rho(i\omega + 2\nu|\mathbf{k}|^2)^2 + (\rho g + \sigma|\mathbf{k}|^2)|\mathbf{k}|}. \end{aligned} \quad (4)$$

We are primarily interested in the wave height, so we proceed by finding $h_1(\mathbf{x})$:

$$\begin{aligned} h_1(\mathbf{x}) &= \frac{F_0}{2\pi\sigma} \int_0^\infty dk \frac{k^2}{(\rho/\sigma)(i\omega + 2\nu k^2)^2 + k/l_c^2 + k^3} J_0(kr) \\ &= \frac{F_0}{2\pi\sigma} \int_0^\infty dk \frac{k^2}{\epsilon^2 k^4 + 2i\epsilon k^2 + k^3 + \beta k - 1} J_0(kk_c r), \end{aligned} \quad (5)$$

where $|\mathbf{x}| = r$, and the capillary length l_c , capillary wave number k_c , reciprocal Reynolds number ϵ , and Bond number β are defined as, respectively,

$$l_c = \sqrt{\frac{\sigma}{\rho g}}, \quad k_c = \left(\frac{\rho\omega^2}{\sigma}\right)^{1/3}, \quad \epsilon = \frac{2\nu k_c^2}{\omega}, \quad \text{and} \quad \beta = \frac{1}{(k_c l_c)^2}. \quad (6)$$

We note that the weakly viscous wave model (1) was derived in Ref. [52] under the assumption $\epsilon \ll 1$. This assumption is satisfied for the experimental parameter regime considered herein, as $0.1 \lesssim \epsilon = 2\nu(\rho/\sigma)^{1/3}\omega^{1/3} \lesssim 0.18$ in the range of forcing frequencies $f = 20\text{--}100$ Hz. We note that, for the sake of simplicity, additional dissipation due to contamination of the free surface by surfactants has been neglected, as was done in prior models [52] that have since been successfully compared to highly controlled experiments [58,59]. Great care is taken in the companion experiments to minimize the presence and influence of surface contaminants [32]. We also note that $\tanh(k_c H) \approx 1$ where H is the bath depth, which justifies taking the bath to be semi-infinite in the z direction.

The integrand in Eq. (5) can be written as

$$\begin{aligned} \frac{k^2}{P(k)} &= \sum_{j=1}^4 \frac{A_j}{k - k_j}, \quad \text{where } P(k) = \epsilon^2 k^4 + 2i\epsilon k^2 + k^3 + \beta k - 1, \\ A_j &= \frac{1}{3 + \beta/k_j^2 + 4i\epsilon/k_j + 4\epsilon^2 k_j}, \end{aligned} \quad (7)$$

TABLE I. Variables and parameters appearing in the wave model (Sec. II) and the trajectory equation for surfers (Sec. IV). Italicized quantities vary with γ and f and so are reported for the typical combination $f = 100$ Hz and $\gamma = 3.3$ g.

Dimensional variable	Definition	Value	Dimensionless variable	Definition	Value
ρ	Fluid density	1.175×10^{-3} g/mm ³	$\epsilon = 2\nu k_c^2/\omega$	Reciprocal Reynolds number	0.18
σ	Fluid surface tension	66 g/s ²	$\beta = 1/(k_c l_c)^2$	Wave Bond number	0.048
η	Fluid dynamic viscosity	0.018 g/(mm s),	k_1	Wave numbers in (7)	$0.96-0.11 i$
$\nu = \eta/\rho$	Fluid kinematic viscosity	15.3 mm ² /s	k_2		$-0.47-1.02 i$
H	Fluid depth	5 mm	k_3		$-0.48+0.78 i$
g	Gravitational acceleration	9810 mm/s ²	k_4		$-31.2+0.36 i$
$f = \omega/2\pi$	Forcing frequency	20–100 Hz	$\mu_{\pm} = m_{\pm}/m$	Mass ratios	0.6, 0.4
$\gamma = \zeta \omega^2$	Forcing acceleration	0–3.5 g	$\mu_0 = \mu_+ - 1/2$	Mass offset	0.1
$l_c = \sqrt{\sigma/\rho g}$	Capillary length	2.39 mm	$\text{Bo} = \rho g R^2/\sigma$	Surfer Bond number	0.2
L	Surfer length	4.3 mm	α [Eq. (16)]	Static force coefficient	0.037
$l = L/2, a$	Surfer half-length, asymmetry	2.15 mm, 1/2	$\tilde{l} = l k_c$	Distance between masses	4.12
$k_c = (\rho \omega^2/\sigma)^{1/3}$	Capillary wave number	1.92 mm ⁻¹	$\xi = \gamma/g$	Forcing acceleration	0–3.5
$\lambda_c = 2\pi/k_c$	Capillary wavelength	3.28 mm	$\tilde{m} = k_c U \tau_v$	Surfer mass	2.23
w	Surfer width	2.7 mm	$\tilde{F}_c = F_c/F_p$	Dynamic force coefficient	2.29×10^4
ρ_s	Surfer density	2.2×10^{-3} g/mm ³			
h_+, h_-	Surfer stern, bow heights	1.2, 0.8 mm			
m	Surfer mass	0.026 g			
$m_+ = aL\rho_s w h_+$	Larger mass	0.015 g			
$m_- = (1-a)L\rho_s w h_-$	Smaller mass	0.01 g			
$R = aL/2$	Surfer effective radius	1.08 mm			
$I = m_+ m_- l^2/m$	Surfer moment of inertia	0.028 g mm ²			
U	Surfer free speed	1.9 mm/s			
$\tau_v = mH/\eta w L$	Viscous timescale	0.61 s			
$F_p = mU/\tau_v$	Propulsive force	0.08 mm · g/s ²			
$F_c = (mg)^2 k_c/\sigma$	Dynamic force coefficient	1.82×10^3 mm · g/s ²			

and $k_j \in \mathbb{C}$ are the roots of $P(k)$. Using the identity (A3) in Appendix A, the integral in Eq. (5) may thus be evaluated explicitly:

$$h_1(\mathbf{x}) = \frac{F_0}{2\pi\sigma} \sum_{j=1}^4 \frac{1}{3 + \beta/k_j^2 + 4i\epsilon/k_j + 4\epsilon^2 k_j} \int_0^\infty dk \frac{J_0(k k_c r)}{k - k_j} = \frac{F_0}{\sigma} \mathcal{H}_d(k_c r),$$

$$\text{where } \mathcal{H}_d(r) = \frac{1}{12} \sum_{j=1}^4 \frac{C_0(-k_j r)}{1 + \beta/3k_j^2 + (4/3)i\epsilon/k_j + (4/3)\epsilon^2 k_j}, \quad C_n(r) = H_n(r) - Y_n(r); \quad (8)$$

H_n is the n th-order Struve function and Y_n the n th-order Bessel function of the second kind [60]. The final solution is

$$h(\mathbf{x}, t) = \text{Re}[h_1(\mathbf{x})e^{i\omega t}] = \text{Re}[h_1(\mathbf{x})] \cos \omega t - \text{Im}[h_1(\mathbf{x})] \sin \omega t. \quad (9)$$

A video of this wave field is shown in Video 1 (left panel), and the wave field corresponding to a pair of point masses is shown in Fig. 3(d).

When implementing the model for interacting capillary surfers (Sec. IV–VI), we numerically compute the roots k_i of $P(k)$. However, analytical insight may be obtained by noting that $\epsilon \ll 1$ and $\beta = O(\epsilon^2)$ for a typical value of the forcing frequency $f = 100$ Hz, as shown in Table I. One can

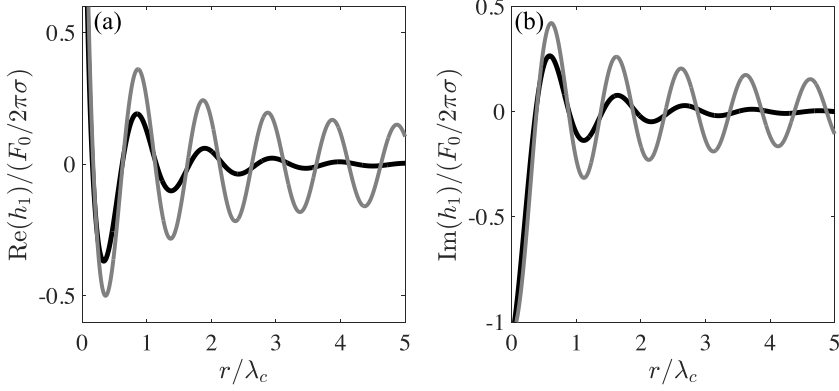


FIG. 2. Real (a) and imaginary (b) parts of the wave height given in Eq. (8) (black curves) are compared against the solution in Eq. (A6) (gray curves), the latter of which neglects viscous and gravitational effects. The parameters correspond to those given in Table I, with forcing frequency $f = 100$ Hz.

then show that the roots of $P(k)$ have the following asymptotic expansions in the limit $\epsilon \rightarrow 0$:

$$k_1 = 1 - \frac{2i\epsilon}{3} + O(\epsilon^2), \quad k_2 = -\varsigma + O(\epsilon), \quad k_3 = -\bar{\varsigma} + O(\epsilon), \quad k_4 = -\frac{1}{\epsilon^2} + O\left(\frac{1}{\epsilon}\right), \quad (10)$$

where $\varsigma = e^{i\pi/3}$. Since $H_0(x)$ and $Y_0(x)$ both vanish as $x \rightarrow \infty$, we thus obtain the following approximation to Eq. (8), valid in the regime $0 < \epsilon \ll 1$, $r \gg \epsilon^2$:

$$h_1(\mathbf{x}) \approx \frac{F_0}{12\sigma} \{\eta_1(r) + 2 \operatorname{Re}[\eta_2(r)]\}, \quad \text{where} \quad \eta_1(r) = C_0 \left[\left(-1 + \frac{2i\epsilon}{3} \right) k_c r \right] \quad \text{and} \\ \eta_2(r) = C_0 [\varsigma k_c r]. \quad (11)$$

While the real part of $\eta_2(r)$ decays monotonically in r , $\eta_1(r)$ decays while oscillating on roughly the capillary wavelength λ_c .

In Appendix A we derive the solution $h_1(\mathbf{x})$ in the absence of gravity and viscosity. The derivation closely follows that of De Corato and Garbin [49]; the significant difference is that we impose the Sommerfeld radiation condition (A7), which enforces that waves propagate outward from the source, while De Corato and Garbin use a reflecting boundary condition at infinity [see Eq. (2.7) in [49]] and thus obtain a standing wave form. Figure 2 shows a comparison between the weakly viscous result (8) and the inviscid result $h_1^+(\mathbf{x})$ in (A6). We observe that, for the typical parameter regime explored in experiments, the inclusion of viscous effects causes $h_1(r)$ to decay faster than its inviscid counterpart. A more detailed discussion of the far-field behavior of h_1 is given in Appendix B. We also note that, since the waves generated by a surfer of mass m have amplitude $A \approx F_0/4\pi\sigma$ where $F_0 \approx m\gamma$ (see Sec. III B), the ratio $A/\lambda_c \approx 0.1$ – 0.3 over the range $f = 20$ – 100 Hz for the largest value of the forcing acceleration considered, $\gamma = 3.5g$, which validates the small-amplitude approximation made in Eq. (1).

III. INTERACTION FORCE BETWEEN A PAIR OF OBJECTS OSCILLATING ON A FLUID INTERFACE

We now derive an approximate expression for the interaction force between a pair of surfers oscillating on the free surface of a fluid. We will use this expression in Sec. IV, where we will propose equations of motion for a collection of surfers that interact pairwise. To our knowledge, there does not exist an analytical expression for the capillary force between two finite-sized objects oscillating on a fluid interface. For this reason, we make the following simplifying approximations. We model a single surfer as a pair of masses, which exert capillary forces on the masses that

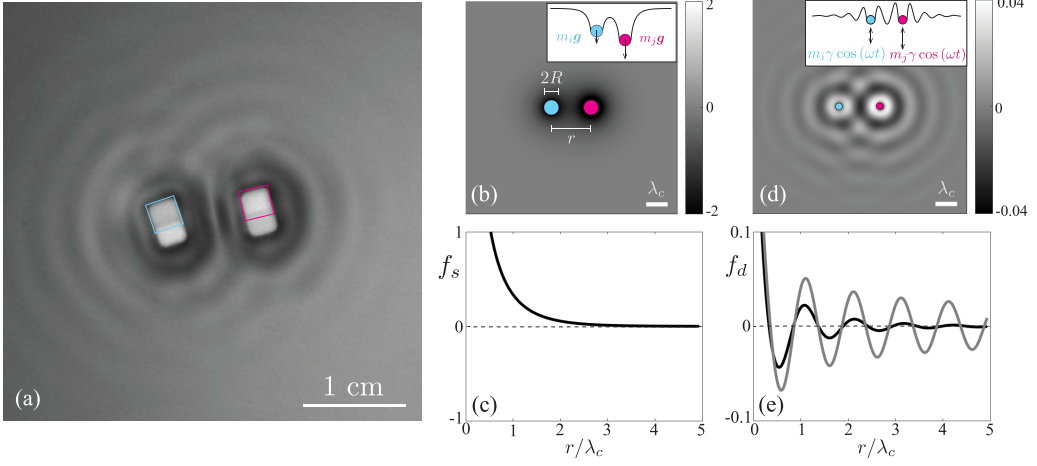


FIG. 3. (a) Experimental image of two surfers [32]. In the theoretical model, each surfer is approximated as a pair of masses. However, for the sake of simplicity we highlight only one mass on each surfer. Specifically, the cyan (magenta) box indicates the front (rear) half of the left (right) surfer. The subsequent panels detail the interactions between the two highlighted masses only. (b) The static force associated with the surfer's weight is approximated by treating each mass as a floating disk of radius $R = L/4$. The color bar indicates the static wave field $(m_i/m)\mathcal{H}_s(k_c|\mathbf{x} - \mathbf{x}_i|) + (m_j/m)\mathcal{H}_s(k_c|\mathbf{x} - \mathbf{x}_j|)$, obtained by superposing the profiles \mathcal{H}_s given in Eq. (16) associated with masses $m_i = 0.4m$ and $m_j = 0.6m$ centered at \mathbf{x}_i and \mathbf{x}_j . (c) The plot shows the dependence of the static force between floating disks f_s on the distance r between the disks, as given in Eq. (17). (d) The dynamic force associated with the surfer's oscillation on the fluid interface is approximated by treating each mass as an oscillating point. The color bar indicates the dynamic wave field due to two masses, $(m_i/m)\text{Re}[\mathcal{H}_d(k_c|\mathbf{x} - \mathbf{x}_i|)] + (m_j/m)\text{Re}[\mathcal{H}_d(k_c|\mathbf{x} - \mathbf{x}_j|)]$, obtained by superposing the profiles \mathcal{H}_d given in Eq. (8). (e) The black curve shows the time-averaged dynamic force f_d between oscillating point masses, as given in Eq. (18). The gray curve shows the corresponding expression (A13) derived in Ref. [49], in which gravitational and viscous effects were neglected. The parameters correspond to those given in Table I, with forcing frequency $f = 100$ Hz. In panels (b) and (d), the insets show the wave field along the horizontal line connecting the masses, and the scale bar indicates the capillary wavelength λ_c .

represent other surfers [Fig. 1(d)]. While each surfer is approximated as a pair of masses, for the sake of simplicity we highlight only one mass on each surfer in Fig. 3(a), with the cyan (magenta) box indicating the front (rear) half of the left (right) surfer. The other panels in Fig. 3 detail the interactions between the two highlighted masses only, while the complete pairwise surfer interaction model (described in Sec. IV) includes the interactions between all four masses. The “static” part of the force, induced by the object's weight, is approximated by treating each mass as a floating disk [Figs. 3(b) and 3(c)]. This force is responsible for the so-called “Cheerios effect” [36], which causes floating objects to clump together. The “dynamic” part of the force, induced by the object's oscillation on the fluid interface, is approximated by treating each mass as an oscillating point particle, which is the problem we solved in Sec. II [Figs. 3(d) and 3(e)]. This approximation is expected to be valid when the distance between surfers is much larger than the surfer's length L . Expressions for the static and dynamic forces are derived in Sec. III A and Sec. III B, respectively.

A. Static force between floating disks

We proceed by calculating the interfacial deformation $h_s(r)$ due to a floating disk of radius R and mass m at rest at a depth χ below the undisturbed free surface. The Young-Laplace equation with Dirichlet boundary conditions,

$$\Delta h_s \equiv h_s'' + \frac{1}{r} h_s' = \frac{h_s}{l_c^2}, \quad r > R, \quad h_s(R) = -\chi, \quad h_s \rightarrow 0 \quad \text{as } r \rightarrow \infty, \quad (12)$$

has the solution [36]

$$h_s(r) = -\chi \frac{K_0(r/l_c)}{K_0(R/l_c)}, \quad (13)$$

where K_0 is the modified Bessel function of the second kind of order zero. The depth χ is calculated by balancing the disk's weight mg against the buoyancy force $\rho g \pi R^2 \chi$ and the vertical component $2\pi R \sigma \sin \theta$ of the surface tension force, θ being the contact angle of the fluid with the disk:

$$mg = \rho g \pi R^2 \chi + 2\pi R \sigma \sin \theta. \quad (14)$$

Assuming $\theta \ll 1$, so that $\sin \theta \approx \tan \theta \approx h'(R)$, we obtain

$$\chi = \frac{mg}{\pi \sigma} \frac{K_0(\sqrt{\text{Bo}})}{\text{Bo} K_0(\sqrt{\text{Bo}}) + 2\sqrt{\text{Bo}} K_1(\sqrt{\text{Bo}})}, \quad (15)$$

where $\text{Bo} \equiv \rho g R^2 / \sigma = (R/l_c)^2$ is the Bond number, and we use the fact that $K'_0 = -K_1$. Substituting Eq. (15) into Eq. (13), we obtain the following formula for the static deformation generated by a floating disk:

$$h_s(r) = -\frac{mg\alpha}{\sigma} \mathcal{H}_s(k_c r), \quad \text{where} \quad \mathcal{H}_s(r) = \frac{1}{\sqrt{\beta}} K_0(\sqrt{\beta} r) \quad \text{and} \quad \alpha = \frac{\sqrt{\beta}}{\pi (\text{Bo} K_0(\sqrt{\text{Bo}}) + 2\sqrt{\text{Bo}} K_1(\sqrt{\text{Bo}}))}. \quad (16)$$

This solution is plotted in Fig. 3(b).

The force \mathbf{F}_{ij}^s on a disk of mass m_i at $\mathbf{x} = \mathbf{x}_i$ due to the static deformation generated by a disk of mass m_j at $\mathbf{x} = \mathbf{x}_j$ is [36]

$$\mathbf{F}_{ij}^s \approx -m_i g \nabla h_s(\mathbf{x} - \mathbf{x}_j)|_{\mathbf{x}=\mathbf{x}_i} = \frac{m_i m_j g^2}{\sigma} \alpha k_c f_s(k_c r_{ij}) \hat{\mathbf{x}}_i^j, \quad \text{where} \quad r_{ij} = |\mathbf{x}_i - \mathbf{x}_j|, \quad \hat{\mathbf{x}}_i^j = \frac{\mathbf{x}_j - \mathbf{x}_i}{r_{ij}}, \quad \text{and} \quad f_s(r) = -\mathcal{H}'_s(r) = K_1(\sqrt{\beta} r). \quad (17)$$

Here we have assumed that the distance between the disks is much bigger than the capillary length, $r_{ij} \gg l_c$. Note that this force is always attractive and decays exponentially with the distance between the objects, as shown in Fig. 3(c).

B. Dynamic force between oscillating point particles

The results of Sec. II can readily be used to compute the force between two point particles with positions (\mathbf{x}_i, z_i) and (\mathbf{x}_j, z_j) , as depicted in Fig. 3(d). Specifically, we assume that the particles oscillate on the fluid interface with the same phase, $\ddot{z}_j = -\zeta_j \omega^2 \cos \omega t$, and compute the time-averaged force \mathbf{F}_{ij}^d on particle i due to the deformation generated by particle j . Following Ref. [49], we use the result that the capillary force on particle i has a lateral component proportional to the gradient of the interfacial deformation generated by particle j [61]. Recalling the definition of h in Eq. (9), we thus obtain

$$\mathbf{F}_{ij}^d = \langle m_i \ddot{z}_i \nabla h(\mathbf{x} - \mathbf{x}_j, t)|_{\mathbf{x}=\mathbf{x}_i} \rangle = \frac{m_i m_j \zeta_i \zeta_j \omega^4}{2\sigma} k_c f_d(k_c r) \hat{\mathbf{x}}_i^j, \quad \text{where} \quad f_d(r) = -\text{Re}[\mathcal{H}'_d(r)] = \frac{1}{12} \sum_{n=1}^4 \text{Re} \left[k_n \frac{H_{-1}(-k_n r_{ij}) + Y_1(-k_n r_{ij})}{1 + \beta/3 k_n^2 + (4/3) i \epsilon / k_n + (4/3) \epsilon^2 k_n} \right], \quad (18)$$

the time average over the oscillation period $2\pi/\omega$ is denoted by $\langle \cdot \rangle$, and we use the facts that $Y'_0 = -Y_1$ and $H'_0 = H_{-1}$. A plot of the dynamic force (18) is shown in Fig. 3(e): while it is attractive

when the particles are close together, $r \ll \lambda_c$, it differs from the static force (17) in that it oscillates between attractive and repulsive as r increases. This net oscillatory interaction force has both stable and unstable equilibria, quantized on the capillary wavelength. This result might be anticipated in cases where standing waves mediate surface interaction, as arise in the bouncing droplet system [24,25] or if reflecting boundary conditions were considered in our system [49]. However, in our case the point sources (and surfers) are sources of continuously generated propagating waves, and thus it is both the wave field and synchronized vertical oscillation that together lead to the apparent spatial quantization predicted by Eq. (18). Note also that Eq. (18), which incorporates the effects of viscosity, decays much faster than its inviscid counterpart (A13), which was derived by De Corato and Garbin [49].

IV. TRAJECTORY EQUATIONS FOR CAPILLARY SURFERS

We proceed by constructing the equations of motion for a collection of interacting surfers, the relevant variables being listed in Table I. Consider a surfer with the “boat” geometry shown in Fig. 1(b), with length L , width w , asymmetry a , stern (bow) heights h_+ (h_-), mass density ρ_s , and mass m , floating on the free surface of a fluid bath oscillating vertically with acceleration γ and frequency ω . Since there does not exist an analytical expression for the force between two surfers oscillating on a fluid interface, we model each surfer as a pair of masses chosen to represent the surfer’s asymmetric mass distribution in experiments, $m_+ = La\rho_s wh_+$ and $m_- = L(1-a)\rho_s wh_-$ [Fig. 1(c)]. These masses are assumed to be nonrotating and connected by a rigid massless rod of length $l = L/2$. For the “static” part of the force, induced by the surfer’s weight, we treat each mass as a disk of radius $R_+ = aL/2$ and $R_- = (1-a)L/2$, where $R_+ = R_- = R \equiv L/4$ for the case $a = 1/2$ considered herein. We use Eq. (17) to approximate the interaction force between two such disks [Figs. 3(b) and 3(c)]. For the “dynamic” part of the force, induced by the surfer’s oscillation on the fluid interface, we treat each mass as a point particle and use Eq. (18) to approximate the interaction force between two point particles [Figs. 3(d) and 3(e)].

We describe the trajectory of the i th surfer by its center of mass $\mathbf{x}_i(t) \in \mathbb{R}^2$ and orientation (unit) vector $\mathbf{n}_i(t)$, which points from m_+ to m_- [Fig. 1(d)]. The masses are centered at $\mathbf{x}_{i,\pm} = \mathbf{x}_i \mp \mu_{\mp} l \mathbf{n}_i$, where $\mu_{\pm} = m_{\pm}/m$. Each mass moves in response to two forces: drag forces $-D_{\pm} \dot{\mathbf{x}}_{i,\pm}$ and wave forces \mathbf{F}_{\pm} , time-averaged over the forcing period $2\pi/\omega$ of the bath. The equations of motion are thus

$$m_{\pm}(\ddot{\mathbf{x}}_i \mp \mu_{\mp} l \ddot{\mathbf{n}}_i) + D_{\pm}(\dot{\mathbf{x}}_i \mp \mu_{\mp} l \dot{\mathbf{n}}_i) = \mathbf{F}_{\pm}. \quad (19)$$

Since the contact line remains pinned to the surfer’s base, the dominant contribution to the drag arises from the viscous shear stress underneath the surfer. We have assumed that the associated drag force is proportional to the velocity $\dot{\mathbf{x}}_{i,\pm}$ of each mass, an approximation that is valid provided that the laminar boundary layer thickness $l_{BL} \approx 5\sqrt{\nu L/U}$ is much greater than the fluid depth H , $l_{BL}/H \gg 1$, U being the surfer’s characteristic speed. We approximate the associated drag coefficient as $D_{\pm} = m_{\pm}/\tau_v$, where $\tau_v = mH/\eta wL$ is the viscous timescale obtained by computing the shear stress due to a locally fully developed Couette flow on the underside of the surfer. Prior experiments [62] on a disk that slides across an air-water interface showed that, in the regime $l_{BL}/H \ll 1$, the drag is dominated by skin friction due to the boundary layer underneath the body, with associated drag force proportional to $U^{3/2}$. We find that $25 \lesssim l_{BL}/H \lesssim 270$ for the experiments considered herein [32], an intermediate regime for which a simple drag law does not exist but the linear drag law is more appropriate. For the sake of simplicity, we neglect the influence of hydrodynamic interactions between the two masses on the values of the drag coefficients.

Adding the two equations in Eq. (19), we obtain the trajectory equation for the center of mass

$$m\left(\ddot{\mathbf{x}}_i + \frac{1}{\tau_v} \dot{\mathbf{x}}_i\right) = \mathbf{F}_+ + \mathbf{F}_-. \quad (20)$$

To model the rotational dynamics, we take the cross product of the first equation in Eq. (19) with $-\mu_- \mathbf{n}_i$, the second equation with $\mu_+ \mathbf{n}_i$, and add the two resulting equations:

$$[m_-(\mu_+ l)^2 + m_+(\mu_- l)^2] \mathbf{n}_i \times \ddot{\mathbf{n}}_i + \frac{1}{\tau_v} [m_-(\mu_+ l)^2 + m_+(\mu_- l)^2] \mathbf{n}_i \times \dot{\mathbf{n}}_i = \mathbf{l} \mathbf{n}_i \times (\mu_+ \mathbf{F}_- - \mu_- \mathbf{F}_+). \quad (21)$$

Writing $\mathbf{n}_i = (\cos \theta_i, \sin \theta_i)$, Eq. (21) reduces to

$$I \ddot{\theta}_i + \frac{I}{\tau_v} \dot{\theta}_i = \mathbf{l} \mathbf{n}_i \times (\mu_+ \mathbf{F}_- - \mu_- \mathbf{F}_+), \quad (22)$$

where $I = m_+(\mu_- l)^2 + m_-(\mu_+ l)^2 = \mu_+ \mu_- m l^2$ is the moment of inertia in the plane.

The wave forces \mathbf{F}_\pm may be decomposed into three terms: a propulsive force due to radiation pressure ($F_p/2 \mathbf{n}_i$), an attractive capillary force (17) due to the surfer's weight, and a dynamic wave force (18) due to the interfacial waves generated by the surfers. The latter two are expressed as a linear superposition of the forces generated by all other surfers, as shown schematically in Fig. 1(d). We thus obtain the trajectory equations

$$\begin{aligned} m \ddot{\mathbf{x}}_i + \frac{m}{\tau_v} \dot{\mathbf{x}}_i &= F_p \mathbf{n}_i + F_c \sum_{p,q=\pm 1} \mu_p \mu_q \sum_{j \neq i} \Phi(k_c |\mathbf{x}_{j,q} - \mathbf{x}_{i,p}|) \frac{\mathbf{x}_{j,q} - \mathbf{x}_{i,p}}{|\mathbf{x}_{j,q} - \mathbf{x}_{i,p}|}, \\ I \ddot{\theta}_i + \frac{I}{\tau_v} \dot{\theta}_i &= -l F_c \sum_{p,q=\pm 1} \mu_p \mu_q \sum_{j \neq i} p \mu_{-p} \Phi(k_c |\mathbf{x}_{j,q} - \mathbf{x}_{i,p}|) \mathbf{n}_i \times \frac{\mathbf{x}_{j,q} - \mathbf{x}_{i,p}}{|\mathbf{x}_{j,q} - \mathbf{x}_{i,p}|}, \end{aligned} \quad (23)$$

where $F_c = (mg)^2 k_c / \sigma$ is the capillary force coefficient. The interaction force Φ is obtained by adding Eqs. (17) and (18), where we assume that the surfer oscillation amplitudes ζ_i are equal to the forcing amplitude γ / ω^2 of the bath:

$$\Phi(r) = \alpha f_s(r) + \frac{\xi^2}{2} f_d(r), \quad \text{where } \xi = \frac{\gamma}{g}. \quad (24)$$

Equations (23) account for the lateral force and torque balances on each surfer, respectively. The trajectory equations contain a single unknown parameter F_p , whose value $F_p = mU / \tau_v$ is directly inferred from the experimentally measured free speed U of a single surfer in isolation. We observe from Table I that $\alpha \ll \xi^2$ for $\gamma / g \geq 1$, the regime in which most of the experiments are conducted [32], indicating that the dynamic force typically dominates the static force. The dynamic wave field, which we will plot in Sec. V, is obtained by combining Eqs. (8), (9), and (16):

$$h(\mathbf{x}, t) = -\frac{mg}{\sigma} \sum_{p=\pm 1} \mu_p \sum_i \mathcal{H}(k_c |\mathbf{x} - \mathbf{x}_{i,p}|, t), \quad \text{where } \mathcal{H}(r, t) = \alpha \mathcal{H}_s(r) + \xi \text{Re}[\mathcal{H}_d(r) e^{i\omega t}]. \quad (25)$$

We proceed by nondimensionalizing the trajectory equations (23) using $\mathbf{x} \rightarrow k_c \mathbf{x}$ and $t \rightarrow tk_c F_p \tau_v / m$:

$$\begin{aligned} \tilde{m} \ddot{\mathbf{x}}_i + \dot{\mathbf{x}}_i &= \mathbf{n}_i + \tilde{F}_c \sum_{p,q=\pm 1} \mu_p \mu_q \sum_{j \neq i} \Phi(|\mathbf{x}_{j,q} - \mathbf{x}_{i,p}|) \frac{\mathbf{x}_{j,q} - \mathbf{x}_{i,p}}{|\mathbf{x}_{j,q} - \mathbf{x}_{i,p}|}, \\ \tilde{m} \ddot{\theta}_i + \tilde{l} \dot{\theta}_i &= -\tilde{F}_c \sum_{p,q=\pm 1} p \mu_q \sum_{j \neq i} \Phi(|\mathbf{x}_{j,q} - \mathbf{x}_{i,p}|) \mathbf{n}_i \times \frac{\mathbf{x}_{j,q} - \mathbf{x}_{i,p}}{|\mathbf{x}_{j,q} - \mathbf{x}_{i,p}|}, \end{aligned} \quad (26)$$

where $\tilde{l} = lk_c$, $\mathbf{x}_{i,p} = \mathbf{x}_i - p \mu_{-p} \tilde{\mathbf{l}} \mathbf{n}_i$, and the dimensionless parameters

$$\tilde{m} = \frac{k_c F_p \tau_v^2}{m} = k_c U \tau_v \quad \text{and} \quad \tilde{F}_c = \frac{F_c}{F_p} = \frac{F_c \tau_v}{mU} \quad (27)$$

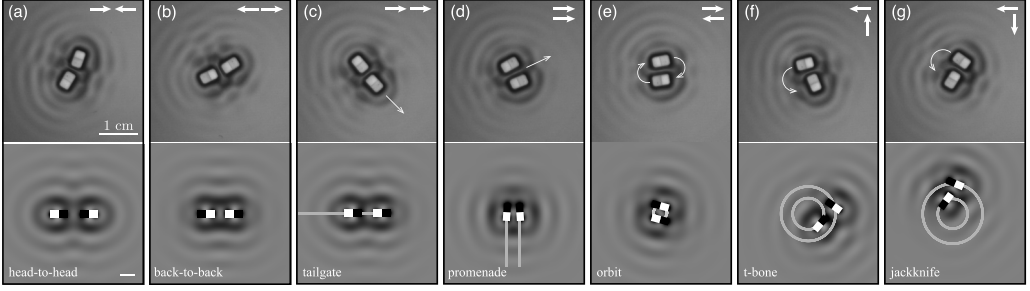


FIG. 4. Bound states of pairs of surfers, obtained in experiment [32] (top row) and numerical simulations of (28) with different initial conditions (bottom row). (a) Head-to-head, (b) back-to-back, (c) tailgate, (d) promenade, (e) orbit, (f) t-bone, and (g) jackknife. The forcing frequency is $f = 100$ Hz and forcing acceleration is $\gamma/g = 3.3$, for which the surfer free speed is $U = 1.9$ mm/s. The values of the parameters are given in Table I. The associated wave fields are given by Eq. (25) evaluated at $t = 0$. Scale bar in numerical simulations denotes the capillary wavelength λ_c .

are defined through the free speed $U = F_p \tau_v / m$ of a single surfer in isolation. Equation (26) is solved using a fourth-order explicit Runge-Kutta method in MATLAB, and the Struve functions in the expression for Φ are evaluated using the toolbox “Struve functions” developed by Theodoulidis [63].

V. BOUND STATES OF PAIRS OF SURFERS

For a pair of surfers, Eq. (26) can be written as

$$\begin{aligned} \tilde{m}\ddot{\mathbf{x}}_1 = & -\dot{\mathbf{x}}_1 + \mathbf{n}_1 + \tilde{F}_c \{ (\mathbf{x}_2 - \mathbf{x}_1) [\mu_+^2 f_{++} + \mu_-^2 f_{--} + \mu_+ \mu_- (f_{+-} + f_{-+})] \\ & + \tilde{l} \mu_+ \mu_- [(\mathbf{n}_1 - \mathbf{n}_2)(\mu_+ f_{++} - \mu_- f_{--}) + \mathbf{n}_1(\mu_- f_{-+} - \mu_+ f_{+-}) + \mathbf{n}_2(\mu_+ f_{-+} - \mu_- f_{+-})] \}, \end{aligned} \quad (28a)$$

$$\begin{aligned} \tilde{m}\ddot{\mathbf{x}}_2 = & -\dot{\mathbf{x}}_2 + \mathbf{n}_2 - \tilde{F}_c \{ (\mathbf{x}_2 - \mathbf{x}_1) [\mu_+^2 f_{++} + \mu_-^2 f_{--} + \mu_+ \mu_- (f_{+-} + f_{-+})] \\ & + \tilde{l} \mu_+ \mu_- [(\mathbf{n}_1 - \mathbf{n}_2)(\mu_+ f_{++} - \mu_- f_{--}) + \mathbf{n}_1(\mu_- f_{-+} - \mu_+ f_{+-}) + \mathbf{n}_2(\mu_+ f_{-+} - \mu_- f_{+-})] \}, \end{aligned} \quad (28b)$$

$$\begin{aligned} \tilde{m}\tilde{l}\ddot{\theta}_1 = & -\tilde{l}\dot{\theta}_1 + \tilde{F}_c \mathbf{n}_1 \times \{ (\mathbf{x}_2 - \mathbf{x}_1) [\mu_+(f_{+-} - f_{++}) - \mu_-(f_{-+} - f_{--})] \\ & + \mu_+ \mu_- \tilde{l} (f_{++} + f_{--} - f_{+-} - f_{-+}) \mathbf{n}_2 \}, \end{aligned} \quad (28c)$$

$$\begin{aligned} \tilde{m}\tilde{l}\ddot{\theta}_2 = & -\tilde{l}\dot{\theta}_2 - \tilde{F}_c \mathbf{n}_2 \times \{ (\mathbf{x}_2 - \mathbf{x}_1) [\mu_+(f_{-+} - f_{++}) - \mu_-(f_{+-} - f_{--})] \\ & - \mu_+ \mu_- \tilde{l} (f_{++} + f_{--} - f_{+-} - f_{-+}) \mathbf{n}_1 \}, \end{aligned} \quad (28d)$$

where $f_{pq} = \Phi(|\delta_{pq}|)/|\delta_{pq}|$ and $\delta_{pq} = \mathbf{x}_{2,p} - \mathbf{x}_{1,q}$; specifically,

$$\begin{aligned} \delta_{++} &= \mathbf{x}_2 - \mathbf{x}_1 - \mu_- \tilde{l} (\mathbf{n}_2 - \mathbf{n}_1), & \delta_{--} &= \mathbf{x}_2 - \mathbf{x}_1 + \mu_+ \tilde{l} (\mathbf{n}_2 - \mathbf{n}_1), \\ \delta_{+-} &= \mathbf{x}_2 - \mathbf{x}_1 - \tilde{l} (\mu_- \mathbf{n}_2 + \mu_+ \mathbf{n}_1), & \text{and } \delta_{-+} &= \mathbf{x}_2 - \mathbf{x}_1 + \tilde{l} (\mu_+ \mathbf{n}_2 + \mu_- \mathbf{n}_1). \end{aligned} \quad (29)$$

Numerical simulations of Eq. (28) demonstrate that our model recovers the seven different interaction modes exhibited by two surfers of equal size and speed (Fig. 4). In the head-to-head mode [Fig. 4(a)] the two surfer bows face each other, while in the back-to-back mode [Fig. 4(b)] the two surfer sterns face each other. While these modes are static, the remaining five modes are dynamic. In the tailgating mode [Fig. 4(c), Video 2], the surfers are aligned along their major axis, with the bow of one surfer pointing toward the stern of the other, and they move with constant speed

along a rectilinear trajectory. In the promenade mode [Fig. 4(d), Video 3], they proceed side by side with constant speed along a rectilinear trajectory. In the orbiting mode [Fig. 4(e), Video 4], the two surfers orbit around the system's fixed center of mass. In the t-bone mode [Fig. 4(f), Video 5], the two major axes are perpendicular to each other and the bow of one surfer points toward the stern of the other, while they both execute a circular trajectory. The jackknife mode [Fig. 4(g), Video 5] has a similar configuration except the stern of one surfer points toward the stern of the other.

We proceed by considering the existence and stability of the bound states shown in Fig. 4, as predicted by the model (28). To that end, we rewrite Eq. (28) in terms of the variables

$$\boldsymbol{\sigma} = \mathbf{x}_1 + \mathbf{x}_2 \quad \text{and} \quad \boldsymbol{\delta} = \mathbf{x}_2 - \mathbf{x}_1. \quad (30)$$

Adding and subtracting Eqs. (28a)–(28b) and Eqs. (28c)–(28d), we obtain

$$m\ddot{\boldsymbol{\sigma}} = -\dot{\boldsymbol{\sigma}} + \mathbf{n}_1 + \mathbf{n}_2, \quad (31a)$$

$$m\ddot{\boldsymbol{\delta}} = -\dot{\boldsymbol{\delta}} + \mathbf{n}_2 - \mathbf{n}_1 - 2\tilde{F}_c[\delta\mathcal{F} + \tilde{l}\mu_+\mu_-(\mathbf{n}_1\mathcal{T}_1 - \mathbf{n}_2\mathcal{T}_2)], \quad (31b)$$

$$m\tilde{l}(\ddot{\theta}_1 + \ddot{\theta}_2) = -\tilde{l}(\dot{\theta}_1 + \dot{\theta}_2) + \tilde{F}_c\boldsymbol{\delta} \times (\mathbf{n}_1\mathcal{T}_1 - \mathbf{n}_2\mathcal{T}_2), \quad (31c)$$

$$m\tilde{l}(\ddot{\theta}_1 - \ddot{\theta}_2) = -\tilde{l}(\dot{\theta}_1 - \dot{\theta}_2) + \tilde{F}_c[\boldsymbol{\delta} \times (\mathbf{n}_1\mathcal{T}_1 + \mathbf{n}_2\mathcal{T}_2) + 2\mu_+\mu_-\tilde{l}\mathbf{S}\mathbf{n}_1 \times \mathbf{n}_2], \quad (31d)$$

where

$$\begin{aligned} \mathcal{F} &= \mu_+^2 f_{++} + \mu_-^2 f_{--} + \mu_+\mu_-(f_{+-} + f_{-+}), \quad \mathcal{S} = f_{++} + f_{--} - f_{+-} - f_{-+}, \\ \mathcal{T}_1 &= \mu_+ f_{++} - \mu_+ f_{+-} + \mu_- f_{-+} - \mu_- f_{--}, \quad \mathcal{T}_2 = \mu_+ f_{++} + \mu_- f_{+-} - \mu_+ f_{-+} - \mu_- f_{--}. \end{aligned} \quad (32)$$

The bound states are determined by the distance between the surfers $d = |\boldsymbol{\delta}|$, and the angles φ_1 and φ_2 between the surfers' orientation vectors \mathbf{n}_i and $\boldsymbol{\delta}$ through the relations $\cos \varphi_i = \mathbf{n}_i \cdot \boldsymbol{\delta}/d$ [Fig. 1(d)]. In Sec. V A we treat the one-dimensional rectilinear modes (head-to-head, back-to-back, tailgating), which are determined by d alone. We then treat the promenade mode in Sec. V B, which is determined by d and φ_2 since $\varphi_1 = \pi - \varphi_2$. We shall see that the promenade speed v is determined by φ_2 . In Sec. V C we treat the rotating modes, which are determined by d , φ_1 and φ_2 , variables that determine the orbital frequency ω_0 . The linear stability analysis of the rectilinear (head-to-head, back-to-back, tailgating, promenading) and rotating (orbiting, t-bone, jackknife) states is presented in Appendixes C 1 and C 2, respectively. We conduct a quantitative comparison between theory and experiment for the promenade mode, the mode that exhibits the largest number of equilibrium spacings for the parameter regime explored in experiments [32].

A. Head-to-head, back-to-back, and tailgating modes

The head-to-head mode [Fig. 4(a)] centered at the origin and oriented along the x axis is given by $\boldsymbol{\sigma} = \mathbf{0}$, $\boldsymbol{\delta} = (d, 0)$ [corresponding to $\mathbf{x}_1 = (-d/2, 0)$, $\mathbf{x}_2 = (d/2, 0)$], $\mathbf{n}_1 = (1, 0)$, and $\mathbf{n}_2 = (-1, 0)$, where d is the distance between the centers of mass. Substituting this solution into Eq. (31) and defining μ_0 through $\mu_{\pm} = 1/2 \pm \mu_0$, we obtain a single algebraic equation that determines d :

$$1 = \tilde{F}_c F_H(d),$$

$$\text{where} \quad F_H(d) = -d(\mu_+^2 f_{++} + \mu_-^2 f_{--} + 2\mu_+\mu_- f_{+-}) - 2\tilde{l}\mu_+\mu_-[\mu_+ f_{++} - \mu_- f_{--} - 2\mu_0 f_{+-}]$$

$$\text{and} \quad |\boldsymbol{\delta}_{++}| = d + 2\mu_-\tilde{l}, \quad |\boldsymbol{\delta}_{--}| = d - 2\mu_+\tilde{l}, \quad |\boldsymbol{\delta}_{+-}| = |\boldsymbol{\delta}_{-+}| = d - 2\tilde{l}\mu_0. \quad (33)$$

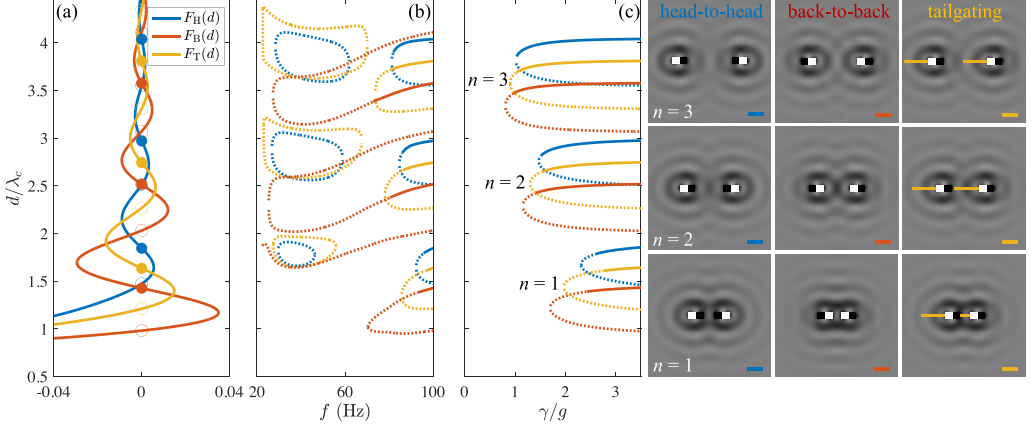


FIG. 5. (a) Force curves corresponding to the head-to-head [blue, Eq. (33)], back-to-back [red, Eq. (34)], and tailgating [yellow, Eq. (35)] modes, for $f = 100$ Hz and $\gamma/g = 3.3$. Filled (unfilled) circles correspond to stable (unstable) solutions. (b) Dependence of the distance d on the forcing frequency f , as described in Sec. V A, for surfer pairs in each of the three modes. Solid (dashed) curves correspond to stable (unstable) solutions. (c) The dependence of the distance d between surfers on the forcing acceleration γ for fixed forcing frequency $f = 100$ Hz. The three rightmost columns show, for the mode order n indicated, the (unique) stable mode for $\gamma/g = 3.3$ and $f = 100$ Hz. The corresponding wave field is computed using Eq. (25) evaluated at $t = 0$, and scale bars denote the capillary wavelength λ_c . Movies of the tailgating modes are shown in Video 2.

Similarly, the back-to-back mode [Fig. 4(b)] is given by $\sigma = \mathbf{0}$, $\delta = (d, 0)$, $\mathbf{n}_1 = (-1, 0)$, and $\mathbf{n}_2 = (1, 0)$, from which we obtain

$$\begin{aligned}
 -1 &= \tilde{F}_c F_B(d), \\
 \text{where } F_B(d) &= -d(\mu_+^2 f_{++} + \mu_-^2 f_{--} + 2\mu_+ \mu_- f_{+-}) \\
 &\quad + 2\tilde{l}\mu_+ \mu_- [\mu_+ f_{++} - \mu_- f_{--} - 2\mu_0 f_{+-}] \quad \text{and} \\
 |\delta_{++}| &= d - 2\mu_- \tilde{l}, \quad |\delta_{--}| = d + 2\mu_+ \tilde{l}, \quad |\delta_{+-}| = |\delta_{-+}| = d + 2\tilde{l}\mu_0.
 \end{aligned} \tag{34}$$

The tailgating mode [Fig. 4(c)] with speed v is given by $\sigma = (vt, 0)$, $\delta = (d, 0)$ [corresponding to $\mathbf{x}_1 = (-d/2 + vt, 0)$, $\mathbf{x}_2 = (d/2 + vt, 0)$], and $\mathbf{n}_1 = \mathbf{n}_2 = (1, 0)$. The first equation in Eq. (31) implies that $v = 1$, or that the speed in the tailgating mode is equal to the surfer free speed, a result that is roughly consistent with experimental data on the $n = 1$ mode (see Table II in Appendix D). The second equation in Eq. (31) reduces to

$$\begin{aligned}
 F_T(d) &= 0, \text{ where } F_T(d) = -d[(\mu_+^2 + \mu_-^2)f_{++} + \mu_+ \mu_- (f_{+-} + f_{-+})] - \tilde{l}\mu_+ \mu_- (f_{-+} - f_{+-}) \\
 \text{and } |\delta_{++}| &= |\delta_{--}| = d, \quad |\delta_{+-}| = d - \tilde{l}, \quad |\delta_{-+}| = d + \tilde{l}.
 \end{aligned} \tag{35}$$

The force curves $F_H(d)$, $F_B(d)$, and $F_T(d)$ are shown in Fig. 5(a). The equilibrium distances d are found numerically using bisection; since $\tilde{F}_c \gg 1$ in the parameter regime of interest (Table I), the equilibrium distances are well approximated by the roots of the functions F_H , F_B , and F_T . The stability of the equilibria is assessed using the framework detailed in Appendix C 1. The dependence of d on the forcing frequency f is shown in Fig. 5(b). As in the experiments [see Fig. 3(f) in [32]], both f and γ (and thus ξ) are varied together; specifically, γ/g increases from 1.1 to 3.3 as f is varied from 50 to 100 Hz. The dimensionless parameters \tilde{m} and \tilde{l} depend on the surfer free speed U , which in turn varies with both γ and f . The values of U and ξ are thus inferred from the experimental data in Fig. S1 of [32] using linear interpolation or extrapolation. The dependence of d on the forcing acceleration γ for a fixed forcing frequency $f = 100$ Hz is shown in Fig. 5(c).

From Figs. 5(b) and 5(c), we observe that, for each of the three modes considered, there is a quantized set of stable solutions (solid lines) separated by unstable ones (dashed lines). Specifically, in the stable head-to-head, back-to-back, and tailgating modes, the centers of mass are separated by roughly integer multiples of the capillary wavelength: $d = n\lambda_c$, $d = (n - 1/2)\lambda_c$, and $d = (n - 1/4)\lambda_c$, respectively, where $n \geq 2$. From Fig. 5(b) [Fig. 5(c)], we observe that stable modes exist over a larger range of f (γ) values as n increases. We also note that, as shown in Fig. 5(b), there are unstable families of solutions at relatively low frequencies ($f < 70$ Hz). The head-to-head and back-to-back equilibria will play a role in the next section, where we discuss the so-called promenade mode.

B. Promenade mode

The promenade mode [Fig. 4(d)], in which surfers move side by side at a constant velocity orthogonal to the line connecting their centers, is given by $\sigma = (0, vt)$, $\delta = (d, 0)$ [corresponding to $\mathbf{x}_1(t) = (-d/2, vt)$, $\mathbf{x}_2(t) = (d/2, vt)$], $\theta_1(t) = \pi - \varphi_2$, and $\theta_2(t) = \varphi_2$. Substituting this solution into Eq. (31) we obtain a system of equations that determines the distance d between surfers, their speed v and orientation φ_2 :

$$v = \sin \varphi_2,$$

$$0 = F_p(d, \varphi_2) \equiv -\cos \varphi_2 + \tilde{F}_c\{(\mu_+^2 f_{++} + \mu_-^2 f_{--} + 2\mu_+\mu_- f_{+-})d - 2\tilde{l}\mu_+\mu_- \cos \varphi_2[\mu_+ f_{++} - \mu_- f_{--} - 2\mu_0 f_{+-}]\},$$

$$0 = T_p(d, \varphi_2) \equiv d[\mu_+ f_{++} - \mu_- f_{--} - 2\mu_0 f_{+-}] - 2\mu_+\mu_- \tilde{l} \cos \varphi_2 (f_{++} + f_{--} - 2f_{+-}),$$

where $|\delta_{++}| = |d - 2\mu_- \tilde{l} \cos \varphi_2|$, $|\delta_{--}| = |d + 2\mu_+ \tilde{l} \cos \varphi_2|$,

$$\text{and } |\delta_{+-}|^2 = |\delta_{-+}|^2 = d^2 + \tilde{l}^2(\mu_+^2 + \mu_-^2 - 2\mu_+\mu_- \cos 2\varphi_2) + 4d\tilde{l}\mu_0 \cos \varphi_2. \quad (36)$$

The first (second) equation in Eq. (36) represents the force balance in the transverse (lateral) direction, while the third equation represents the torque balance. The distinct promenade modes are found numerically by finding the roots of $F_p(d, \varphi_2)$ and $T_p(d, \varphi_2)$, which constitutes a system of two equations in two unknowns. Specifically, we compute the zero contours of the two functions using MATLAB and locate their intersections [64], as depicted in Fig. 12 in Appendix C. The stability of the solutions is assessed using the framework described in Appendix C 1. We assume that $v \geq 0$ and thus restrict our attention to $0 \leq \varphi_2 \leq \pi$.

The dependence of the equilibrium distance d and orientation angle φ_2 on the forcing frequency f is shown in Fig. 6. As in Fig. 5(b), both f and γ are varied together, with the intermediate values extrapolated from the experimental data as detailed in Sec. V A and the caption of Fig. 6. We observe that the stable (solid curves) promenade modes are roughly quantized on the capillary wavelength, with separation distance $d \approx n\lambda_c$ for $n \in \mathbb{N}$. The stable states have angle $\varphi_2 \gtrsim \pi/2$, indicating that the surfers are approximately oriented along their direction of motion. The model also predicts a number of unstable (dashed curves) solutions with a variety of separation distances and angles. The stable equilibrium distances exhibit excellent agreement with experiment, with the theory correctly capturing the slight decrease in d/λ_c with increasing f . The agreement between theory and experiment improves at lower values of f , presumably because the quasipotential approximation for the wave field in Eq. (1) is valid for $\epsilon \ll 1$, and the reciprocal Reynolds number scales as $\epsilon \sim \omega^{1/3}$ from Eq. (6). We note that, for the experimental data points in Fig. 6, the surfer width w is subtracted from d . This correction accounts for the fact that, while a surfer is represented as a pair of point sources in the model, experimental observations indicate that a surfer generates waves along its whole perimeter. We also note that, as f is varied for $n = 2, 3$, and 4, most of the solution branches bifurcate into the head-to-head (blue) and back-to-back (red) modes as $\varphi_2 \rightarrow \pi^-$ and $\varphi_2 \rightarrow 0^+$, respectively.

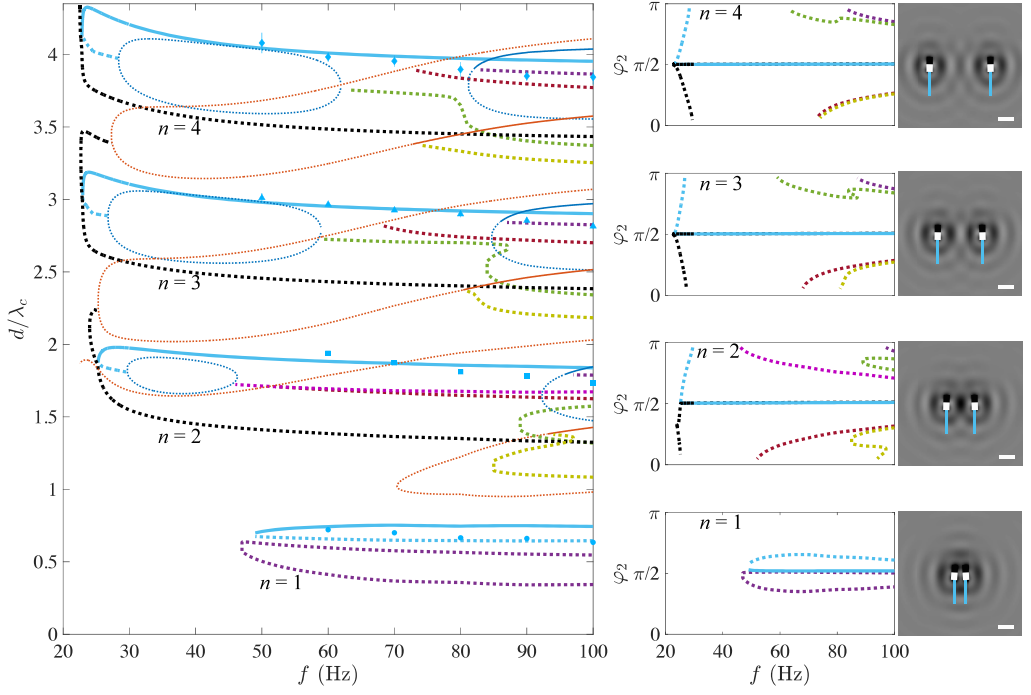


FIG. 6. Dependence of the promenade mode equilibria on the forcing frequency f , as obtained by solving Eq. (36) using the procedure described in Sec. VB. The large panel shows the dependence on f of the distance d between the surfers' centers of mass. Stable (unstable) promenade mode solutions are indicated by the solid (dashed) curves. Data points correspond to the values of $d - w$ obtained in experiments [see Fig. 3(f) in [32]], the w term accounting for the surfers' finite width. In the experiments, f ranges from 50 to 100 Hz in increments of 10 Hz, and the corresponding values of γ/g are 1.1, 1.5, 2.0, 2.3, 3.0, and 3.3. The head-to-head (blue) and back-to-back (red) modes from Fig. 5(b) are superimposed. The middle column shows the corresponding orientation angle φ_2 for the mode order n indicated. For a given mode order, the colors correspond to those in the large panel. The rightmost column shows, for each n , the (unique) stable promenade mode for the combination $f = 100$ Hz and $\gamma/g = 3.3$, and the corresponding wave field (25) evaluated at $t = 0$. Scale bars denote the capillary wavelength λ_c . Movies of these promenade modes are shown in Video 3.

The dependence of the promenade speed on f , where both f and γ are varied together as in Fig. 6, is shown in the left column of Fig. 13 (Appendix D), while the dependence of the promenade speed on γ for fixed $f = 100$ Hz is shown in the right column. Since $v = \sin \varphi_2$ and $\varphi_2 \gtrsim \pi/2$, the theory predicts that the speed of stable promenade modes is just slightly less than the free speed of a single surfer, and the dimensionless promenade speed v/U is roughly constant ($\lesssim 1$) across a range of values of f and γ . These two predictions agree with experiment when the surfers are relatively far apart, in the $n = 3$ and $n = 4$ modes; however, when the surfers are relatively close together, as in the $n = 1$ and $n = 2$ modes, the promenade speed can go down to as low as 50% of the free speed in experiment, a phenomenon not captured by the theoretical model. A similar quantitative discrepancy was observed in a study on oil droplets that bounce on the surface of a vertically vibrating fluid bath, pairs of which also executed the promenade mode [65]. In that study, the discrepancy was resolved by modeling the coupling between the droplets' horizontal and vertical dynamics. While the surfer model presented herein neglects consideration of the vertical dynamics, presumably an analogous extension of the model would lead to predicted promenade speeds that are closer to those observed in experiments. Furthermore, both the static and dynamic components to the present model improve as approximations when the surfers are spaced farther apart, and thus some

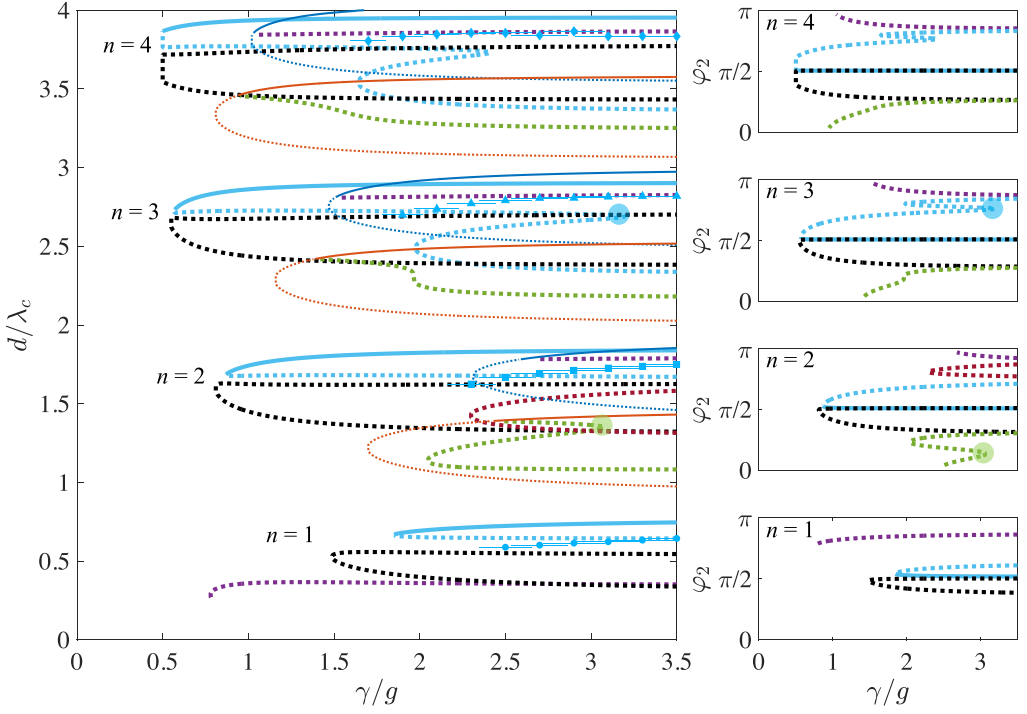


FIG. 7. Dependence of the promenade mode equilibria on the forcing acceleration γ , for the fixed forcing frequency $f = 100$ Hz. The head-to-head (blue) and back-to-back (red) modes from Fig. 5(c) are superimposed. Data points correspond to the values of $d - w$ obtained in experiments [see Fig. 3(e) in [32]]. See the caption of Fig. 6 for more details.

quantitative disagreement between experiment and theory might be anticipated when the surfers are relatively close to one another, as in the smallest n modes.

Figure 7 shows the dependence of the equilibrium distance d and orientation angle φ_2 on the forcing acceleration γ for the forcing frequency $f = 100$ Hz, the largest value of f considered in experiments. The predicted equilibrium distances d exhibit adequate agreement with experiment, and correctly capture a number of trends: namely, that d is quantized on the capillary wavelength λ_c and remains slightly below integer multiples of λ_c ; d increases very slightly with forcing acceleration γ ; and that the critical γ above which stable promenade solutions appear decreases with the mode order n , as was the case with the head-to-head, back-to-back, and tailgating modes [Fig. 5(c)]. However, the theoretically predicted values of d are systematically larger than those obtained in experiment, presumably due to the fact that the quasipotential approximation is less accurate at larger frequencies. We note that, for $\gamma \approx 3g$, the theory predicts two small regions of “exotic” promenade modes, highlighted by the green and blue circles, where $d/\lambda_c \approx 1.25$ and 2.75 and $\varphi_2 \approx \pi/8$ and $3\pi/4$, respectively. These exotic states coexist with the other promenade modes and presumably exist in a corner of parameter space too small to be accessed by experiments.

C. Orbiting, jackknife and t-bone modes

Circular orbit solutions, in which two surfers traverse a circular orbit with constant angular frequency ω_0 , are given by the expressions $\delta = d(\cos \omega_0 t, \sin \omega_0 t)$, $\mathbf{n}_1 = (\cos(\omega_0 t + \varphi_1), \sin(\omega_0 t + \varphi_1))$, and $\mathbf{n}_2 = (\cos(\omega_0 t + \varphi_2), \sin(\omega_0 t + \varphi_2))$. We substitute this solution into Eq. (31). To simplify the resulting system of equations, we take the cross product of δ with Eq. (31b) and add to it the

product of Eq. (31c) and $2\mu_+\mu_-\tilde{l}$:

$$\omega_0(d^2 + 4\mu_+\mu_-\tilde{l}^2) = d(\sin \varphi_2 - \sin \varphi_1) \Rightarrow \omega_0 = \frac{d(\sin \varphi_2 - \sin \varphi_1)}{d^2 + 4\mu_+\mu_-\tilde{l}^2}. \quad (37)$$

We then take the cross product of Eq. (31b) with $(\mathbf{n}_1\mathcal{T}_1 - \mathbf{n}_2\mathcal{T}_2)$ and add to it the product of Eq. (31c) and $2\mathcal{F}$:

$$-\tilde{m}\omega_0^2d(\mathcal{T}_1 \sin \varphi_1 - \mathcal{T}_2 \sin \varphi_2) - d\omega_0(\mathcal{T}_1 \cos \varphi_1 - \mathcal{T}_2 \cos \varphi_2) + (\mathcal{T}_1 - \mathcal{T}_2) \sin(\varphi_2 - \varphi_1) = -4\tilde{l}\omega_0\mathcal{F}. \quad (38)$$

Equation (31c) reduces to

$$2\omega_0\tilde{l} = \tilde{F}_c d(\mathcal{T}_1 \sin \varphi_1 - \mathcal{T}_2 \sin \varphi_2), \quad (39)$$

while Eq. (31d) reduces to

$$d(\mathcal{T}_1 \sin \varphi_1 + \mathcal{T}_2 \sin \varphi_2) + 2\mu_+\mu_-\tilde{l}\mathcal{S} \sin(\varphi_2 - \varphi_1) = 0. \quad (40)$$

Using Eq. (29), \mathcal{F} , \mathcal{S} , \mathcal{T}_1 , and \mathcal{T}_2 are evaluated using the formulas

$$\begin{aligned} |\delta_{++}|^2 &= d^2 + \left(2\tilde{l}\mu_- \sin \frac{\varphi_2 - \varphi_1}{2}\right)^2 - 2d\tilde{l}\mu_-(\cos \varphi_2 - \cos \varphi_1), \\ |\delta_{--}|^2 &= d^2 + \left(2\tilde{l}\mu_+ \sin \frac{\varphi_2 - \varphi_1}{2}\right)^2 + 2d\tilde{l}\mu_+(\cos \varphi_2 - \cos \varphi_1), \\ |\delta_{+-}|^2 &= d^2 + \tilde{l}^2[\mu_+^2 + \mu_-^2 + 2\mu_+\mu_- \cos(\varphi_2 - \varphi_1)] - 2d\tilde{l}(\mu_+ \cos \varphi_1 + \mu_- \cos \varphi_2), \\ |\delta_{-+}|^2 &= d^2 + \tilde{l}^2[\mu_+^2 + \mu_-^2 + 2\mu_+\mu_- \cos(\varphi_2 - \varphi_1)] + 2d\tilde{l}(\mu_- \cos \varphi_1 + \mu_+ \cos \varphi_2). \end{aligned} \quad (41)$$

Using Eq. (37) to eliminate ω_0 , the system of three equations (38)–(40) thus defines the three unknowns d , φ_1 , and φ_2 . The stability of circular orbits is assessed using the framework described in Appendix C 2.

The orbiting mode [Fig. 4(e)] is a special case in which the surfers orbit their fixed center of mass while remaining diametrically opposed to each other. Equation (40) is trivial in this mode, since $\varphi_2 - \varphi_1 = \pi$ and thus $|\delta_{+-}| = |\delta_{-+}|$, so $\mathcal{T}_1 = \mathcal{T}_2$. After using Eq. (37), Eqs. (38) and (39) make up a system of two equations in the two unknowns d and φ_2 , which may be solved using the method described in Sec. VB. We assume that the surfers orbit in the counterclockwise sense ($\omega_0 > 0$), and thus restrict our attention to $0 \leq \varphi_2 \leq \pi$.

The dependence of d and φ_2 on the forcing acceleration γ is shown in Fig. 8. As with the promenade mode (Fig. 7), we observe that the stable (solid curves) orbiting modes are roughly quantized on the capillary wavelength, with separation distance $d \approx n\lambda_c$ for $n \in \mathbb{N}$. The stable states have angle $\varphi_2 \gtrsim \pi/2$, indicating that the surfers remain roughly tangent to the circle they traverse. As with the promenade mode, for $n = 2, 3$, and 4, two branches of unstable orbiting modes bifurcate into the head-to-head (blue) and back-to-back (red) modes as $\varphi_2 \rightarrow \pi^-$ and $\varphi_2 \rightarrow 0^+$, respectively. Using Eq. (37), we deduce that the orbital speed $d\omega_0/2$ increases with orbit order n and remains less than unity, the free speed of a single surfer. While the orbital speeds in the $n = 1$ and $n = 2$ modes, respectively, are predicted to be roughly 60% and 90% of the free speed, in experiments they are slightly greater than the free speed (see Table II in Appendix D).

In the t-bone [Fig. 4(f)] and jackknife [Fig. 4(g)] modes, two surfers execute circular orbits of different radii around a common center. We locate these modes by solving Eqs. (38)–(40) for the three unknowns d , φ_1 , and φ_2 . The contour method described in Sec. VB is designed for two unknowns and thus cannot be used; we instead use MATLAB's root-finding algorithm to locate some of the modes, and leave the identification of all possible t-bone and jackknife modes for future work. The dependence of d , φ_1 , and φ_2 on the forcing acceleration γ is shown in Fig. 9. We observe that stable t-bone (jackknife) modes satisfy $\varphi_1 \lesssim 0$ ($\varphi_1 \lesssim \pi$), and both satisfy $\varphi_2 \approx \pi/2$. As with

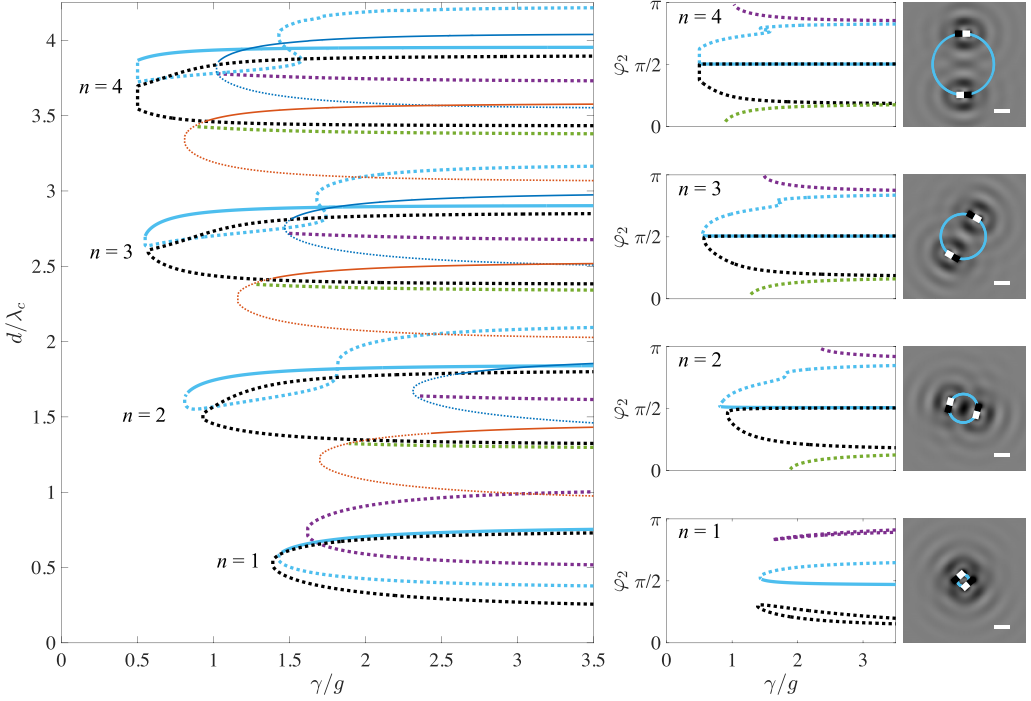


FIG. 8. Orbiting modes of surfer pairs, obtained by solving Eqs. (38) and (39) for the orbital diameter d and orientation angle $\varphi_2 = \varphi_1 + \pi$. The large panel shows the dependence of d on the forcing acceleration γ . Stable (unstable) orbiting modes are indicated by the solid (dashed) curves. The head-to-head (blue) and back-to-back (red) modes from Fig. 5(b) are superimposed. The middle column shows φ_2 for the mode order indicated. For a given mode order n , curves of the same color indicate the same solution branch. The rightmost column shows, for each n , the (unique) stable orbiting mode for $\gamma/g = 3.3$ and the corresponding wave field (25) evaluated at $t = 0$. Scale bars denote the capillary wavelength λ_c . Movies of these orbiting modes are shown in Video 4.

the orbiting modes (Fig. 8), the distance d between surfers is quantized on the capillary wavelength, with the t-bone modes consistently larger than the jackknife modes.

The trajectories and wave fields in the third and fourth columns of Fig. 9 are obtained by recasting the solutions in terms of $\mathbf{x}_1 = (\boldsymbol{\sigma} - \boldsymbol{\delta})/2$ and $\mathbf{x}_2 = (\boldsymbol{\sigma} + \boldsymbol{\delta})/2$. Specifically, we let $\boldsymbol{\sigma} \equiv s(\cos(\omega_0 t + \psi), \sin(\omega_0 t + \psi))$ and find s and ψ by numerically solving the system of equations

$$-\tilde{m}s\omega_0^2 = \cos(\varphi_2 - \psi) + \cos(\varphi_1 - \psi), \quad s\omega_0 = \sin(\varphi_2 - \psi) + \sin(\varphi_1 - \psi), \quad (42)$$

which are obtained from Eq. (31a). Moreover, the orbital diameter $d_1 = |\mathbf{x}_1|/2$ and $d_2 = |\mathbf{x}_2|/2$ of each surfer may be deduced using the relations

$$d_1 = \sqrt{d^2 + s^2 - 2ds \cos \psi}, \quad d_2 = \sqrt{d^2 + s^2 + 2ds \cos \psi},$$

from which the orbital velocities $v_1 = d_1\omega_0/2$ and $v_2 = d_2\omega_0/2$ follow directly. Experimental data on the orbital velocities are available for both t-bone and jackknife $n = 1$ modes, and for the jackknife $n = 2$ mode, for the single-parameter combination $f = 100$ Hz and $\gamma/g = 3.3$ (see Table II in Appendix D). For the t-bone mode, if we take the upper (lower) limits of the velocity range measured experimentally for the inner (outer) surfer, we find that the predicted velocities agree to within 10%. However, there is a larger discrepancy between theory and experiment for the jackknife modes, as the velocity of the inner surfer is markedly underpredicted.

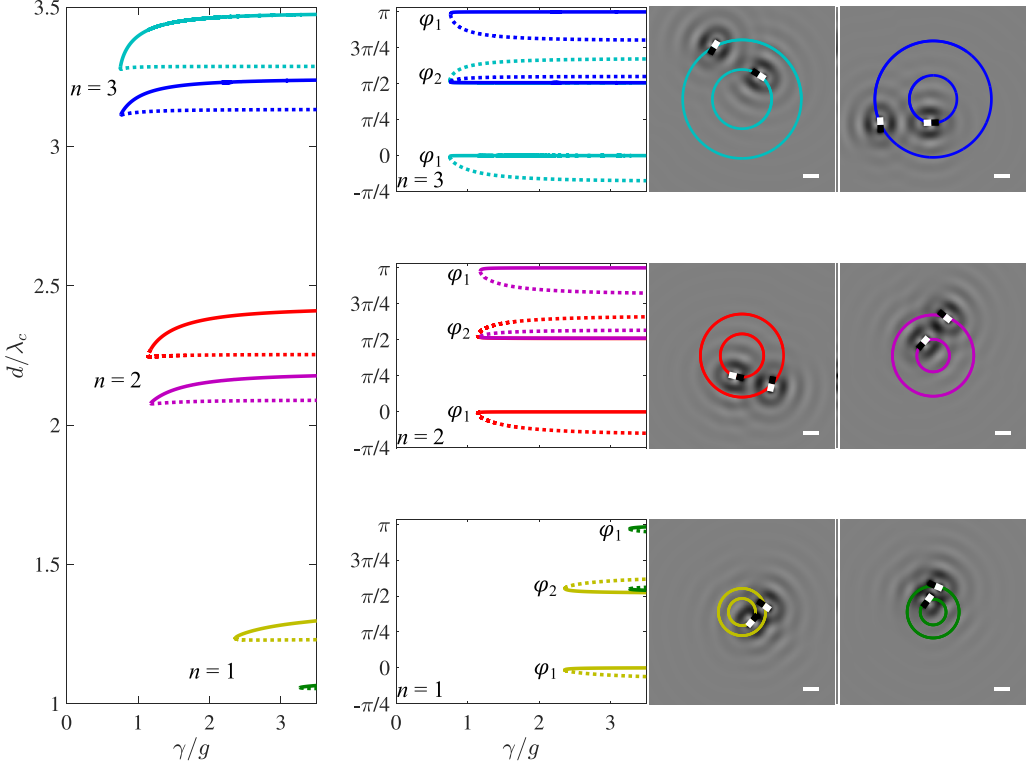


FIG. 9. T-bone (yellow, red, cyan) and jackknife (green, magenta, blue) modes, as obtained by solving Eqs. (38)–(40) for the forcing frequency $f = 100$ Hz. Stable (unstable) states are indicated by the solid (dashed) lines. The left column shows the dependence of the distance d between surfers on the forcing acceleration γ . The panels in the second column show the corresponding orientation angles φ_1 and φ_2 for each mode order n indicated. The third (fourth) columns show, for each n , the stable t-bone (jackknife) mode for $\gamma/g = 3.3$ and the corresponding wave field (25) evaluated at $t = 0$. Scale bars denote the capillary wavelength λ_c . Movies of these t-bone and jackknife modes are shown in Video 5.

VI. COLLECTIVE MODES

Experiments and simulations of our model (26) show that collections of capillary surfers exhibit unique self-organization phenomena. For example, a many-body promenade mode has been observed in experiment [Fig. 4(a) in [32]] and simulations [Fig. 10(a), Video 6]. Similarly, simulations are able to reproduce the “super-orbiting mode” [Fig. 10(b), Video 7], wherein eight surfers execute orbital motion around a fixed center of mass [Fig. 4(b) in [32]]. Owing to its simplicity, the theoretical model is also able to produce more exotic collective modes that are currently difficult to realize in experiments. For example, Fig. 10(c) (Video 8) shows an exotic promenade mode of 13 surfers, in which the spacing between neighboring surfers is approximately either one or two capillary wavelengths. This mode may be thus interpreted as an aggregate of $n = 1$ and $n = 2$ promenade modes (Fig. 6) and exhibits an example of how the multistable quantized states obtained in Sec. V can be used as building blocks for many-body states. Figure 10(d) (Video 9) shows a similar phenomenon, wherein a square lattice of 16 surfers executes a coherent flocking state with constant velocity. This state may be interpreted as a combination of the $n = 3$ tailgating (Fig. 5) and promenade modes.

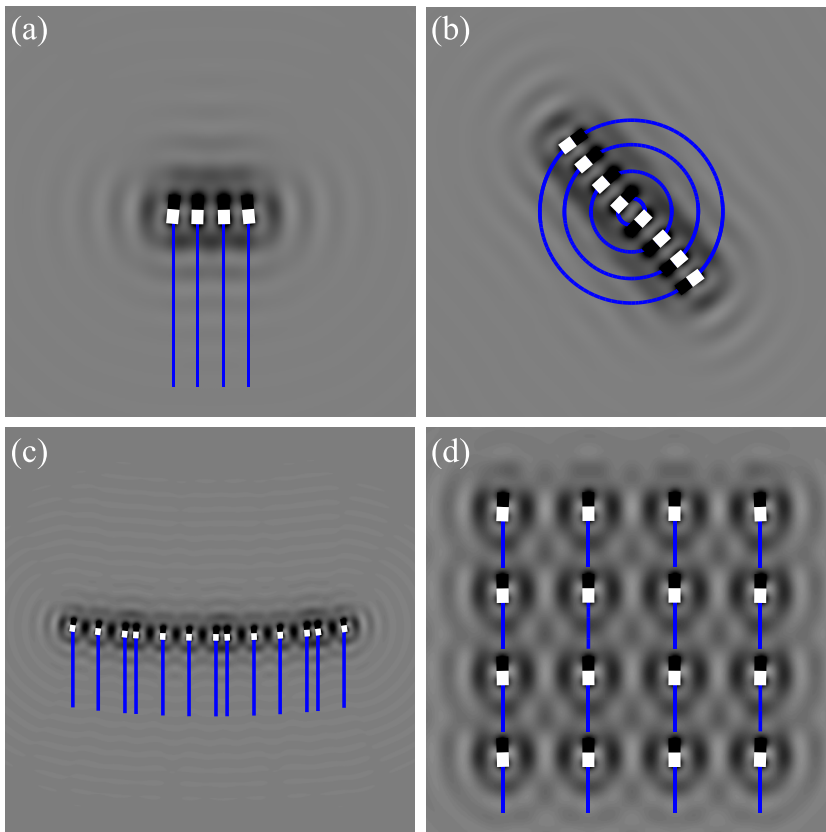


FIG. 10. Collective modes of capillary surfers obtained through numerical simulations of Eq. (26). (a) Four-surfer promenade mode, where the surfers translate at constant velocity and neighbors are separated by approximately one capillary wavelength. (b) Eight-surfer super-orbiting mode, where the collective executes uniform circular motion at constant angular frequency and neighbors are separated by approximately one capillary wavelength. (c) Flocking state of 13 surfers, wherein the collective moves upward with constant velocity. Pairs of surfers are separated by approximately one or two capillary wavelengths. (d) A flocking state of 16 surfers, in which the collective moves with constant velocity. Neighboring surfers are separated by approximately three capillary wavelengths in both the horizontal and vertical directions. All four modes are obtained for the parameter combination $f = 100$ Hz and $\gamma/g = 3.3$. These four modes are shown in Videos 6 through 9, respectively.

VII. CONCLUSION

We have presented a theoretical model (23) for the dynamics of capillary surfers (Fig. 1), bodies that self-propel while oscillating at the interface of a fluid bath. The interfacial deformation generated by such a body is calculated by splitting it into static and dynamic contributions, the former resulting from the body's weight and the latter from the prescribed oscillation of the body at the interface. The static contribution [Eq. (17), Fig. 3(c)] to the force is obtained in Sec. III A by approximating the surfer as a pair of floating disks with unequal masses. The dynamic contribution to the force [Eq. (18), Fig. 3(e)] is obtained in Sec. III B by approximating the surfer as a pair of point sources of weakly viscous gravity-capillary waves, the point-source approximation being required because there does not exist a formula for the dynamic interfacial deformation generated by a finite-sized oscillating body. The resulting formula for the dynamic force is obtained by making use of the results in Sec. II, in which we solved the quasipotential wave model (1) and thus derived

a formula [Eq. (8), Figs. 2(a) and 2(b)] for the small-amplitude (linear) wave field generated by an oscillating point source. In contrast to the static force, the dynamic force has a distinct oscillatory behavior, with stable equilibria quantized by the capillary wavelength. The waves generated by each individual point source are outwardly propagating, and thus the time-averaged surface gradient experienced by each individual particle vanishes. However, the synchronized vertical oscillation of each point source leads to a weighted sampling of the underlying surface gradient, the time-averaged result of which is a spatially oscillatory interaction force. This mechanism reveals the origin of the quantized spacings readily observed in experiment for all stable interaction modes.

The resulting model contains as its only free parameter the speed of a single surfer U , which is obtained from experiment [32]. For the case of two surfers, the model recovers the seven bound states observed in experiments [32] (Fig. 4). We found exact solutions for the head-to-head, back-to-back, and tailgating modes in Sec. V A and investigated their stability in Appendix C 1. These solutions are quantized on the capillary wavelength λ_c , with stable branches of solutions separated by unstable ones (Fig. 5). An exact solution for the promenade mode is found in Sec. V B, and the theoretical predictions correctly capture the trends observed in experiment. Moreover, the theoretically predicted dependence of the distance between surfers on the forcing frequency is in excellent quantitative agreement with experiment (Fig. 6). However, the predicted dependence of the distance on the forcing acceleration for a relatively large value of the forcing frequency ($f = 100$ Hz) exhibits small but systematic discrepancies with experiment (Fig. 7). This is presumably due to the fact that the quasipotential approximation for the wave field is valid in the low-frequency regime $\epsilon \ll 1$. We also found exact solutions for the orbiting (Fig. 8), jackknife, and t-bone (Fig. 9) modes in Sec. V C and investigated their stability in Appendix C 2.

While the theoretically predicted distances between promenading surfers exhibit good agreement with experiment, the promenade speed exhibits less good agreement (Fig. 13 in Appendix D). Specifically, the model typically overpredicts the promenade speed and fails to capture the substantial decrease in speed observed in experiment for the most tightly bound modes ($n = 1$ and $n = 2$). The data shown in Table II in Appendix D for the tailgate, orbit, t-bone, and jackknife mode velocities also exhibit discrepancies between theory and experiment. As discussed in Sec. V B, these discrepancies can presumably be attributed to the fact that our theoretical model neglects modulations in the surfers' vertical dynamics. Indeed, in prior work it was observed that pairs of oil droplets bouncing on the surface of a vertically vibrating fluid can execute both the promenade [65] and orbiting [66] modes; moreover, it was found that neglecting consideration of the droplets' vertical dynamics led to substantial discrepancies between theory and experiment for the droplet speeds, a deficiency that was overcome by modeling the coupling between the droplets' horizontal and vertical dynamics. Furthermore, the simplified static model used here assumes surfer spacings much greater than the capillary length: the approximation of a surfer as two disks for the static force neglects fine-scale geometric details such as edge effects that are relevant for objects floating near each other [67], and the point-source dynamic model is likely to break down near the finite-size surfer. Future extensions to the model to better account for near-field interactions may thus improve the comparison with experiment. Nevertheless, the highly tractable and computationally efficient first interaction model presented herein does predict many of the salient and subtle features observed in the experiment.

All of the bound states described in Sec. V exhibit multistability of a discrete set of interaction states, wherein a number of states quantized on the capillary wavelength may stably coexist for the same experimental parameters. This feature is due to the wave-mediated interactions between surfers, which result in long-range spatially oscillatory forces defined by alternating regions of attraction and repulsion [Fig. 3(e)]. Such interactions give rise to the collective modes shown in Fig. 10, which may be viewed as combinations of pairwise bound states.

While the point force approximation is expected to be valid when the distance between surfers is much larger than the surfer's length, many of the bound states and collective modes reported in experiments consist of closely separated surfers [32]. A promising future direction would thus be to develop a theory for the dynamic deformation generated by a finite-sized body oscillating on

a fluid interface. A theory for dynamically floating bodies may also shed light on the propulsion mechanism of surfers, thus allowing us to eliminate the *ad hoc* propulsive force $F_p \mathbf{n}_i$ in our model (23). We note that, as a consequence of modeling the surfer as a pair of masses, the translational and rotational drag coefficients are equal to each other in the model [see Eqs. (20) and (22)]. This is not true in general for distributed bodies, so a future direction would be to calculate the drag coefficients for the surfer geometry considered in experiment. Another future direction would be to model the surfer's vertical dynamics, which was not considered herein; rather, we simply assumed for the sake of simplicity [between Eqs. (23) and (24)] that the surfer's vertical acceleration is equal to that of the bath. Consideration of the surfer's vertical dynamics would allow us to determine the dependence of the lateral force between surfers on the bath's forcing frequency f and acceleration γ . Moreover, Fig. 10 describes only a small sample of the rich variety of collective modes expected to arise in the surfer system. The self-organization and emergent collective behavior exhibited by large populations of surfers will be detailed in future work.

ACKNOWLEDGMENTS

A.O. acknowledges support from the Simons Foundation (Collaboration Grant for Mathematicians, Award No. 587006) and NSF DMS-2108839. D.M.H. acknowledges support from the Office of Naval Research (ONR N00014-21-1-2816) and the Brown Undergraduate Teaching and Research Award. Special thanks to Prof. Adri Olde Daalhuis for assisting with the argument given in Appendix B, and to Jack-William Barotta for useful discussions.

APPENDIX A: INVISCID LINEAR WAVES GENERATED BY AN OSCILLATING POINT SOURCE

We here derive the linear wave field generated by a point force oscillating harmonically on the free surface of an inviscid fluid bath in the absence of gravity, a problem first considered by De Corato and Garbin [49]. The derivation proceeds as in Sec. II, with the reciprocal Reynolds number and wave Bond numbers set to zero, $\epsilon = \beta = 0$. Equation (5) then reads

$$h_1(\mathbf{x}) = \frac{F_0}{2\pi\sigma} \int_0^\infty dk \frac{k^2}{k^3 - 1} J_0(kk_c r). \quad (\text{A1})$$

Following Appendix A in [49], we compute the integral by rewriting the rational function in the integrand above,

$$\frac{k^2}{k^3 - 1} = \frac{1}{3} \left(\frac{1}{k - 1} + \frac{1}{k + \varsigma} + \frac{1}{k + \bar{\varsigma}} \right), \quad (\text{A2})$$

and using the fact that [68],

$$\int_0^\infty \frac{J_0(kk_c r)}{k + k_0} dk = \frac{\pi}{2} C_0(k_0 k_c r) \quad \text{for } k_0 \in \mathbb{C} \text{ with } \text{Im}(k_0) \neq 0. \quad (\text{A3})$$

However, the integral $\int_0^\infty J_0(kk_c r)/(k - 1) dk$ is divergent. To make sense of the integral, we employ the limiting absorption principle and interpret it as the following limit:

$$\begin{aligned} \lim_{\epsilon \rightarrow 0^+} \int_0^\infty \frac{J_0(kk_c r)}{k - 1 \pm i\epsilon} dk &= \lim_{\epsilon \rightarrow 0^+} \frac{\pi}{2} C_0((-1 \mp i\epsilon)k_c r) \\ &= \lim_{\epsilon \rightarrow 0^+} \frac{\pi}{2} \{-H_0[(1 \pm i\epsilon)k_c r] - Y_0[(1 \pm i\epsilon)k_c r] \mp 2iJ_0[(1 \pm i\epsilon)k_c r]\} \\ &= -\frac{\pi}{2} [H_0(k_c r) + Y_0(k_c r)] \mp i\pi J_0(k_c r), \end{aligned} \quad (\text{A4})$$

where we use the facts [69]

$$H_0(-z) = -H_0(z) \quad \text{and} \quad Y_0(-z) = Y_0(z) - 2i \operatorname{sgn}(\operatorname{Im}[z])J_0(z) \quad \text{for } z \in \mathbb{C} \text{ with } \operatorname{Im}[z] \neq 0. \quad (\text{A5})$$

We thus obtain

$$h_1^\pm(\mathbf{x}) = \frac{F_0}{12\sigma} \{2 \operatorname{Re}[C_0(\varsigma k_c r)] - H_0(k_c r) - Y_0(k_c r) \mp 2iJ_0(k_c r)\}. \quad (\text{A6})$$

We note that the imaginary term is missing from Eq. (3.16) in Ref. [49].

To choose the correct sign in Eq. (A6), we use the Sommerfeld radiation condition, which ensures that the waves propagate outward from the source:

$$\lim_{r \rightarrow \infty} \sqrt{r} \left(\frac{\partial}{\partial r} + ik_c \right) h_1^\pm = 0. \quad (\text{A7})$$

Substituting Eq. (A6) into (A7), we obtain

$$\begin{aligned} \lim_{r \rightarrow \infty} \sqrt{r} \{ -2 \operatorname{Re}[\varsigma C_1(\varsigma k_c r)] + H_1(k_c r) + Y_1(k_c r) \pm 2iJ_1(k_c r) \\ + i\{2 \operatorname{Re}[C_0(\varsigma k_c r)] - H_0(k_c r) - Y_0(k_c r) \mp 2iJ_0(k_c r)\} \} = 0, \end{aligned} \quad (\text{A8})$$

where we use the facts that $Y'_0 = -Y_1$ and $H'_0 = H_{-1} = 2/\pi - H_1$. Using the far-field asymptotic results [69]

$$C_0(z) \sim \frac{2}{\pi z} \quad \text{and} \quad C_1(z) \sim \frac{2}{\pi} \left(1 + \frac{1}{z^2} \right) \quad \text{as } |z| \rightarrow \infty \quad \text{in } |\arg z| < \pi, \quad (\text{A9})$$

Eq. (A8) reduces to

$$\lim_{r \rightarrow \infty} \sqrt{r} \{ Y_1(k_c r) \pm iJ_1(k_c r) - i[Y_0(k_c r) \pm iJ_0(k_c r)] \} = 0. \quad (\text{A10})$$

Using the asymptotic forms for the Bessel function,

$$J_n(x) \sim \sqrt{\frac{2}{\pi x}} \cos\left(x - \frac{\pi}{4} - \frac{n\pi}{2}\right) \quad \text{and} \quad Y_n(x) \sim \sqrt{\frac{2}{\pi x}} \sin\left(x - \frac{\pi}{4} - \frac{n\pi}{2}\right) \quad \text{as } x \rightarrow \infty, \quad (\text{A11})$$

we deduce that Eq. (A10) is satisfied for the solution with the positive sign; that is, $h_1^+(\mathbf{x})$ satisfies the radiation condition (A7). Using Eq. (9), we conclude that the wave field has the form

$$h(\mathbf{x}, t) = \frac{F_0}{12\sigma} \{ [2 \operatorname{Re}[C_0(\varsigma k_c r)] - H_0(k_c r) - Y_0(k_c r)] \cos \omega t + 2J_0(k_c r) \sin \omega t \}. \quad (\text{A12})$$

We note that our result differs from that of Ref. [49] due to the sine term [see Eq. (3.17) there]. That is, the wave form in Ref. [49] is a standing wave due to the authors' assumption of a reflecting boundary condition at infinity [see Eq. (2.7) there]; however, our radiation condition (A7) enforces the requirement that waves propagate outward from the source, which is evident from Video 1 (right panel). Moreover, by combining Eqs. (11) and (A5), it is evident that the wave form (8) that we derived for weakly viscous gravity-capillary waves reduces to $h_1^+(\mathbf{x})$ in Eq. (A6) if the effects of gravity ($\beta = 0$) and viscosity ($\epsilon \rightarrow 0$) are neglected.

We conclude by computing the time-averaged force exerted by one oscillating particle on another: specifically, suppose particles (labeled 0 and 1) separated by a distance r exert vertical forces $F_0 \cos \omega t$ and $F_1 \cos(\omega t + \phi_1)$ on the fluid interface. The force on particle 1 due to the interfacial deformation generated by particle 0 is

$$\begin{aligned} \langle F_1 \cos(\omega t + \phi_1) \nabla h(\mathbf{x}, t) \rangle = \frac{F_0 F_1 k_c}{24\sigma} \{ [2 \operatorname{Re}[\varsigma C_1(\varsigma k_c r)] - H_1(k_c r) - Y_1(k_c r)] \cos \phi_1 \\ - 2J_1(k_c r) \sin \phi_1 \} \hat{\mathbf{r}}, \end{aligned} \quad (\text{A13})$$

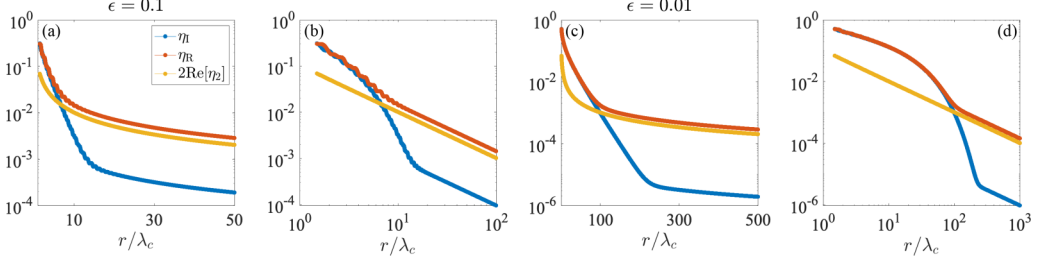


FIG. 11. Plots of the functions $\eta_I(r)$, $\eta_R(r)$ and $2 \operatorname{Re}[\eta_2(r)]$, as defined by Eqs. (B1) and (11). Panels (a) and (b) correspond to $\epsilon = 0.1$, and (c) and (d) to $\epsilon = 0.01$. In each pair, the panel on the left (right) is on semilogarithmic (logarithmic) scale to illustrate the far-field behavior of each function.

where $\hat{\mathbf{r}}$ is a unit vector that points from particle 1 to 0. If the particles oscillate in-phase ($\phi_1 = 0$) or out of phase ($\phi_1 = \pi$), we recover the expression derived in Ref. [49] [see Eq. (3.20) therein]; however, other phase relationships will result in deviations from that expression owing to the J_1 term in Eq. (A13).

APPENDIX B: FAR-FIELD BEHAVIOR OF THE WAVE FIELD GENERATED BY AN OSCILLATING POINT SOURCE IN THE SMALL VISCOSITY LIMIT

We now consider the far-field behavior of the wave field $h_1(r)$ in the regime where viscous effects are small but nonzero ($0 < \epsilon \ll 1$). An approximation of h_1 is given by Eq. (11), and we wish to compare the magnitudes of the two terms $\eta_1(r)$ and $\eta_2(r)$. We observe that $\operatorname{Re}[\eta_2]$ decreases monotonically in r (Fig. 11). Since the real and imaginary parts of η oscillate between positive and negative values, we instead consider their local amplitudes

$$\eta_R(r) = \left(\frac{2}{\lambda_c} \int_{r-\lambda_c/2}^{r+\lambda_c/2} \{\operatorname{Re}[\eta_1(r')]\}^2 dr' \right)^{1/2} \quad \text{and} \quad \eta_I(r) = \left(\frac{2}{\lambda_c} \int_{r-\lambda_c/2}^{r+\lambda_c/2} \{\operatorname{Im}[\eta_1(r')]\}^2 dr' \right)^{1/2}, \quad (\text{B1})$$

which are shown in Fig. 11 for two different values of ϵ . First, we note that $\operatorname{Re}(\eta_2)$ decays algebraically in r , as expected from Eq. (A9), and that $\operatorname{Re}(\eta_2)$ is dominated by η_R and η_I in the region $1 \leq r/\lambda_c \ll 1/\epsilon$. Second, while η_1 also decays algebraically as $r \rightarrow \infty$, we are interested in its behavior for small ϵ , which corresponds to $\arg z_\epsilon \approx \pi$ for $z_\epsilon = (-1 + 2i\epsilon/3)k_c r$. The connection formula (A5) implies that

$$\eta_1(r) = -C_0 \left[\left(1 - \frac{2i\epsilon}{3} \right) k_c r \right] - 2i H_0^{(2)} \left[\left(1 - \frac{2i\epsilon}{3} \right) k_c r \right], \quad (\text{B2})$$

where $H_0^{(2)}$ is the Hankel function of order zero of the second kind (not to be confused with the Struve function). The Hankel function dominates over C_0 for small ϵ and $k_c r = O(1)$, and its asymptotic behavior is given by [69]

$$H_0^{(2)}(z) \sim \sqrt{\frac{2}{\pi z}} \exp[-i(z - \pi/4)] \quad \text{as } |z| \rightarrow \infty. \quad (\text{B3})$$

From Eqs. (B2) and (B3), we conclude that η_1 decays exponentially in the region $r/\lambda_c = O(1/\epsilon)$ and algebraically thereafter, which is confirmed by Fig. 11. We also observe that viscosity damps the waves generated by the point source, since the decay length $3\lambda_c/4\pi\epsilon = 3\lambda_c^3\omega/4(2\pi)^3\nu$ is inversely proportional to the viscosity ν .

APPENDIX C: LINEAR STABILITY ANALYSIS OF BOUND STATES OF SURFER PAIRS

Here we perform the linear stability analysis of rectilinear (Appendix C 1) and rotating (Appendix C 2) bound states. It is useful to use Eq. (30) to write Eq. (28) in the form

$$\tilde{m}\ddot{\boldsymbol{\sigma}} = -\dot{\boldsymbol{\sigma}} + \mathbf{n}_1 + \mathbf{n}_2, \quad (\text{C1a})$$

$$\tilde{m}\ddot{\boldsymbol{\delta}} = -\dot{\boldsymbol{\delta}} + \mathbf{n}_2 - \mathbf{n}_1 - 2\tilde{F}_c[\mu_+^2\mathbf{F}_{++} + \mu_+\mu_-(\mathbf{F}_{+-} + \mathbf{F}_{-+}) + \mu_-^2\mathbf{F}_{--}], \quad (\text{C1b})$$

$$\tilde{m}\tilde{l}\ddot{\theta}_1 = -\tilde{l}\dot{\theta}_1 + \tilde{F}_c\mathbf{n}_1 \times [\mu_+(\mathbf{F}_{+-} - \mathbf{F}_{++}) - \mu_-(\mathbf{F}_{-+} - \mathbf{F}_{--})], \quad (\text{C1c})$$

$$\tilde{m}\tilde{l}\ddot{\theta}_2 = -\tilde{l}\dot{\theta}_2 - \tilde{F}_c\mathbf{n}_2 \times [\mu_+(\mathbf{F}_{-+} - \mathbf{F}_{++}) - \mu_-(\mathbf{F}_{+-} - \mathbf{F}_{--})], \quad (\text{C1d})$$

where

$$\mathbf{F}_{pq} = f_{pq}\boldsymbol{\delta}_{pq} = \frac{\Phi(|\boldsymbol{\delta}_{pq}|)}{|\boldsymbol{\delta}_{pq}|}\boldsymbol{\delta}_{pq}, \quad p, q = + \text{ or } -. \quad (\text{C2})$$

Given a base state \mathbf{x}° and perturbation $\tilde{\mathbf{x}}$, an object that will show up repeatedly is

$$\frac{\Phi(|\mathbf{x}^\circ + \epsilon\tilde{\mathbf{x}}|)}{|\mathbf{x}^\circ + \epsilon\tilde{\mathbf{x}}|}(\mathbf{x}^\circ + \epsilon\tilde{\mathbf{x}}) = \frac{\Phi(|\mathbf{x}^\circ|)}{|\mathbf{x}^\circ|}\mathbf{x}^\circ + \epsilon\mathcal{L}(\mathbf{x}^\circ)\tilde{\mathbf{x}} + O(\epsilon^2),$$

$$\text{where } \mathcal{L}(\mathbf{x}) = \frac{\Phi(|\mathbf{x}|)}{|\mathbf{x}|} \frac{\mathbf{x}^\perp \mathbf{x}^\perp}{|\mathbf{x}|^2} + \Phi'(|\mathbf{x}|) \frac{\mathbf{x}\mathbf{x}}{|\mathbf{x}|^2} \quad (\text{C3})$$

and $\mathbf{x}^\perp = (x, y)^\perp = (-y, x)$. The derivative of the dimensionless force is $\Phi'(r) = \alpha f'_s(r) + (\xi^2/2)f'_d(r)$, where, from Eqs. (17) and (18),

$$f'_s(r) = \sqrt{\beta}K'_1(\sqrt{\beta}r) \quad \text{and} \quad f'_d(r) = -\frac{1}{12} \sum_{j=1}^4 \text{Re} \left[k_j^2 \frac{H'_1(-k_j r) + Y'_1(-k_j r)}{1 + \beta/3k_j^2 + (4/3)i\epsilon/k_j + (4/3)\epsilon^2k_j} \right]. \quad (\text{C4})$$

To evaluate Eq. (C4), we use the identities

$$K'_1(x) = -\frac{1}{2}[K_0(x) + K_2(x)],$$

$$Y'_1(x) = \frac{1}{2}[Y_0(x) - Y_2(x)], \quad \text{and} \quad H'_{-1}(x) = \frac{1}{\pi x} + \frac{1}{2}[H_{-2}(x) - H_0(x)]. \quad (\text{C5})$$

1. Rectilinear modes

We linearize Eq. (C1) around the base state $(\mathbf{x}_i^\circ, \theta_i^\circ)$ for $i = 1, 2$, where $\mathbf{n}_i = (\cos \theta_i, \sin \theta_i)$. To that end, we substitute the expressions $\mathbf{x}_i = \mathbf{x}_i^\circ + \epsilon\tilde{\mathbf{x}}_i$ and $\theta_i = \theta_i^\circ + \epsilon\tilde{\theta}_i$ into Eq. (C1) and retain terms at leading order in ϵ . Using the fact that $\mathbf{n}_i = \mathbf{n}_i^\circ + \epsilon\mathbf{n}_i^{\circ\perp}\tilde{\theta}_i + O(\epsilon^2)$, we obtain the linearized equations of motion

$$\tilde{m} \frac{d^2 \tilde{\boldsymbol{\sigma}}}{dt^2} = -\frac{d\tilde{\boldsymbol{\sigma}}}{dt} + \mathbf{n}_1^{\circ\perp} \tilde{\theta}_1 + \mathbf{n}_2^{\circ\perp} \tilde{\theta}_2,$$

$$\tilde{m} \frac{d^2 \tilde{\boldsymbol{\delta}}}{dt^2} = -\frac{d\tilde{\boldsymbol{\delta}}}{dt} + \mathbf{n}_2^{\circ\perp} \tilde{\theta}_2 - \mathbf{n}_1^{\circ\perp} \tilde{\theta}_1 - 2\tilde{F}_c[\mu_+^2 \mathbb{L}_{++} \tilde{\boldsymbol{\delta}}_{++} + \mu_+\mu_-(\mathbb{L}_{+-} \tilde{\boldsymbol{\delta}}_{+-} + \mathbb{L}_{-+} \tilde{\boldsymbol{\delta}}_{-+}) + \mu_-^2 \mathbb{L}_{--} \tilde{\boldsymbol{\delta}}_{--}],$$

$$\tilde{m}\tilde{l} \frac{d^2 \tilde{\theta}_1}{dt^2} = -\tilde{l} \frac{d\tilde{\theta}_1}{dt} + \tilde{F}_c \{ \mathbf{n}_1^\circ \times [\mu_+(\mathbb{L}_{+-} \tilde{\boldsymbol{\delta}}_{+-} - \mathbb{L}_{++} \tilde{\boldsymbol{\delta}}_{++}) - \mu_-(\mathbb{L}_{-+} \tilde{\boldsymbol{\delta}}_{-+} - \mathbb{L}_{--} \tilde{\boldsymbol{\delta}}_{--})]$$

$$+ \tilde{\theta}_1 \mathbf{n}_1^{\circ\perp} \times [\mu_+(\mathbf{F}_{+-}^\circ - \mathbf{F}_{++}^\circ) - \mu_-(\mathbf{F}_{-+}^\circ - \mathbf{F}_{--}^\circ)] \},$$

$$\begin{aligned} \tilde{m}\tilde{l}\frac{d^2\tilde{\theta}_2}{dt^2} = & -\tilde{l}\frac{d\tilde{\theta}_2}{dt} - \tilde{F}_c\{\mathbf{n}_2^\circ \times [\mu_+(\mathbb{L}_{-+}\tilde{\delta}_{-+} - \mathbb{L}_{++}\tilde{\delta}_{++}) - \mu_-(\mathbb{L}_{+-}\tilde{\delta}_{+-} - \mathbb{L}_{--}\tilde{\delta}_{--})] \\ & + \tilde{\theta}_2\mathbf{n}_2^{\circ\perp} \times [\mu_+(\mathbf{F}_{-+}^\circ - \mathbf{F}_{++}^\circ) - \mu_-(\mathbf{F}_{+-}^\circ - \mathbf{F}_{--}^\circ)]\}. \end{aligned} \quad (\text{C6})$$

Here $\delta_{pq} = \delta_{pq}^\circ + \epsilon\tilde{\delta}_{pq} + O(\epsilon^2)$, $\mathbf{F}_{pq}^\circ = \Phi(|\delta_{pq}^\circ|)\delta_{pq}^\circ/|\delta_{pq}^\circ|$ and $\mathbb{L}_{pq} = \mathcal{L}(\delta_{pq}^\circ)$, where, from Eq. (29),

$$\begin{aligned} \tilde{\delta}_{++} &= \tilde{\delta} - \mu_- \tilde{l}(\mathbf{n}_2^{\circ\perp}\tilde{\theta}_2 - \mathbf{n}_1^{\circ\perp}\tilde{\theta}_1), & \tilde{\delta}_{--} &= \tilde{\delta} + \mu_+ \tilde{l}(\mathbf{n}_2^{\circ\perp}\tilde{\theta}_2 - \mathbf{n}_1^{\circ\perp}\tilde{\theta}_1), \\ \tilde{\delta}_{+-} &= \tilde{\delta} - \tilde{l}(\mu_- \mathbf{n}_2^{\circ\perp}\tilde{\theta}_2 + \mu_+ \mathbf{n}_1^{\circ\perp}\tilde{\theta}_1), & \tilde{\delta}_{-+} &= \tilde{\delta} + \tilde{l}(\mu_+ \mathbf{n}_2^{\circ\perp}\tilde{\theta}_2 + \mu_- \mathbf{n}_1^{\circ\perp}\tilde{\theta}_1). \end{aligned} \quad (\text{C7})$$

We note that Eq. (C6) is independent of the (rescaled) center of mass $\tilde{\sigma}$ due to translation invariance of the governing equations. Equation (C6) may thus be written in the matrix form (dropping the tildes)

$$\begin{aligned} \frac{dz}{dt} &= \mathcal{M}z, \quad \text{where } z = (\delta \quad \dot{\sigma} \quad \dot{\delta} \quad \theta_1 \quad \theta_2 \quad \omega_1 \quad \omega_2)^T \quad \text{and} \\ \mathcal{M} &= \begin{pmatrix} \mathbb{Z} & \mathbb{Z} & \mathbb{I} & \mathbb{Z} & \mathbb{Z} \\ \mathbb{Z} & -\mathbb{I}/\tilde{m} & \mathbb{Z} & \mathbb{N} & \mathbb{Z} \\ \mathbb{F}_1 & \mathbb{Z} & -\mathbb{I}/\tilde{m} & \mathbb{F}_2 & \mathbb{Z} \\ \mathbb{Z} & \mathbb{Z} & \mathbb{Z} & \mathbb{Z} & \mathbb{I} \\ \mathbb{T}_1 & \mathbb{Z} & \mathbb{Z} & \mathbb{T}_2 & -\mathbb{I}/\tilde{m} \end{pmatrix}. \end{aligned} \quad (\text{C8})$$

Here \mathbb{Z} and \mathbb{I} are the 2×2 zero and identity matrices, respectively. The 2×2 matrix \mathbb{F}_1 is defined as

$$\mathbb{F}_1 = -\frac{2\tilde{F}_c}{\tilde{m}}[\mu_+^2\mathbb{L}_{++} + \mu_+\mu_-(\mathbb{L}_{+-} + \mathbb{L}_{-+}) + \mu_-^2\mathbb{L}_{--}], \quad (\text{C9})$$

and the 2×2 matrices

$$\mathbb{N} = \frac{1}{\tilde{m}}(\mathbf{n}_1^{\circ\perp} \quad \mathbf{n}_2^{\circ\perp}), \quad \mathbb{F}_2 = (\mathbf{m}_1 \quad \mathbf{m}_2), \quad \mathbb{T}_1 = \begin{pmatrix} \mathbf{m}_3^T \\ \mathbf{m}_4^T \end{pmatrix}, \quad \text{and} \quad \mathbb{T}_2 = \begin{pmatrix} m_5 & m_6 \\ m_6 & m_7 \end{pmatrix} \quad (\text{C10})$$

are made up of the elements

$$\begin{aligned} \mathbf{m}_1 &= -(\mathbb{I} + 2\tilde{F}_c\tilde{l}\mu_+\mu_-[\mu_+(\mathbb{L}_{++} - \mathbb{L}_{+-}) + \mu_-(\mathbb{L}_{-+} - \mathbb{L}_{--})])\frac{\mathbf{n}_1^{\circ\perp}}{\tilde{m}}, \\ \mathbf{m}_2 &= (\mathbb{I} + 2\tilde{F}_c\tilde{l}\mu_+\mu_-[\mu_+(\mathbb{L}_{++} - \mathbb{L}_{-+}) + \mu_-(\mathbb{L}_{+-} - \mathbb{L}_{--})])\frac{\mathbf{n}_2^{\circ\perp}}{\tilde{m}}, \\ \mathbf{m}_3^T &= \frac{\tilde{F}_c}{\tilde{m}\tilde{l}}(\mathbf{n}_1^{\circ\perp})^T[\mu_+(\mathbb{L}_{+-} - \mathbb{L}_{++}) - \mu_-(\mathbb{L}_{-+} - \mathbb{L}_{--})], \\ \mathbf{m}_4^T &= -\frac{\tilde{F}_c}{\tilde{m}\tilde{l}}(\mathbf{n}_2^{\circ\perp})^T[\mu_+(\mathbb{L}_{-+} - \mathbb{L}_{++}) - \mu_-(\mathbb{L}_{+-} - \mathbb{L}_{--})], \\ m_5 &= \frac{\tilde{F}_c}{\tilde{m}\tilde{l}}\{\tilde{l}\mathbf{n}_1^\circ \times [-\mu_+(\mu_+\mathbb{L}_{+-} + \mu_-\mathbb{L}_{++}) - \mu_-(\mu_-\mathbb{L}_{-+} + \mu_+\mathbb{L}_{--})]\mathbf{n}_1^{\circ\perp} \\ &\quad + \mathbf{n}_1^{\circ\perp} \times [\mu_+(\mathbf{F}_{-+}^\circ - \mathbf{F}_{++}^\circ) - \mu_-(\mathbf{F}_{+-}^\circ - \mathbf{F}_{--}^\circ)]\}, \\ m_6 &= \frac{\tilde{F}_c}{\tilde{m}}\mu_+\mu_-\mathbf{n}_1^\circ \times (-\mathbb{L}_{+-} + \mathbb{L}_{++} - \mathbb{L}_{-+} + \mathbb{L}_{--})\mathbf{n}_2^{\circ\perp}, \\ m_7 &= -\frac{\tilde{F}_c}{\tilde{m}\tilde{l}}\{\tilde{l}\mathbf{n}_2^\circ \times [\mu_+(\mu_+\mathbb{L}_{-+} + \mu_-\mathbb{L}_{++}) + \mu_-(\mu_-\mathbb{L}_{+-} + \mu_+\mathbb{L}_{--})]\mathbf{n}_2^{\circ\perp} \\ &\quad + \mathbf{n}_2^{\circ\perp} \times [\mu_+(\mathbf{F}_{-+}^\circ - \mathbf{F}_{++}^\circ) - \mu_-(\mathbf{F}_{+-}^\circ - \mathbf{F}_{--}^\circ)]\}. \end{aligned} \quad (\text{C11})$$

For each of the rectilinear bound states considered in this paper, the matrix \mathcal{M} has a zero eigenvalue due to the solution's rotational invariance (Appendix C 1 a). The stability of the bound state is thus determined by the remaining eigenvalues; a solution is stable if all of the eigenvalues have negative real part, and is unstable otherwise.

a. Rotational invariance of rectilinear bound states

We proceed by showing that the vector

$$\mathbf{v} = (\delta^{\circ\perp} \quad \mathbf{n}_1^{\circ\perp} + \mathbf{n}_2^{\circ\perp} \quad \mathbf{0} \quad \mathbf{1} \quad \mathbf{0})^T, \quad \text{where } \mathbf{0} = (0, 0) \text{ and } \mathbf{1} = (1, 1) \quad (\text{C12})$$

is in the nullspace of \mathcal{M} , due to the invariance of the governing equations under rotation. The vectors \mathbf{v} and $\mathcal{M}\mathbf{v}$ are in \mathbb{R}^{10} and may be viewed as lists with five entries in \mathbb{R}^2 . We have

$$\mathcal{M}\mathbf{v} = (\mathbf{0} \quad \mathbf{0} \quad \mathbb{F}_1\delta^{\circ\perp} + \mathbb{F}_2\mathbf{1} \quad \mathbf{0} \quad \mathbb{T}_1\delta^{\circ\perp} + \mathbb{T}_2\mathbf{1})^T, \quad (\text{C13})$$

where the second entry vanishes because $\mathbb{N}\mathbf{1} = (\mathbf{n}_1^{\circ\perp} + \mathbf{n}_2^{\circ\perp})/\tilde{m}$. The third entry is, after some algebra and using the fact that $\mathbb{L}_{pq}\delta_{pq}^{\circ\perp} = \mathbf{F}_{pq}^{\circ\perp}$,

$$\begin{aligned} \mathbb{F}_1\delta^{\circ\perp} + \mathbf{m}_1 + \mathbf{m}_2 &= \frac{\mathbf{n}_2^{\circ\perp} - \mathbf{n}_1^{\circ\perp}}{\tilde{m}} - \frac{2\tilde{F}_c}{\tilde{m}} [\mu_+^2 \mathbb{L}_{++}\delta_{++}^{\circ\perp} + \mu_+\mu_-(\mathbb{L}_{+-}\delta_{+-}^{\circ\perp} + \mathbb{L}_{-+}\delta_{-+}^{\circ\perp}) \\ &\quad + \mu_-^2 \mathbb{L}_{--}\delta_{--}^{\circ\perp}] \\ &= \frac{\mathbf{n}_2^{\circ\perp} - \mathbf{n}_1^{\circ\perp}}{\tilde{m}} - \frac{2\tilde{F}_c}{\tilde{m}} [\mu_+^2 \mathbf{F}_{++}^{\circ\perp} + \mu_+\mu_-(\mathbf{F}_{+-}^{\circ\perp} + \mathbf{F}_{-+}^{\circ\perp}) + \mu_-^2 \mathbf{F}_{--}^{\circ\perp}], \end{aligned} \quad (\text{C14})$$

which is zero by Eq. (C1b). The last entry in Eq. (C13) is

$$\mathbb{T}_1\delta^{\circ\perp} + \mathbb{T}_2\mathbf{1} = \begin{pmatrix} \mathbf{m}_3 \cdot \delta^{\circ\perp} + m_5 + m_6 \\ \mathbf{m}_4 \cdot \delta^{\circ\perp} + m_6 + m_7 \end{pmatrix}, \quad (\text{C15})$$

where

$$\begin{aligned} \mathbf{m}_3 \cdot \delta^{\circ\perp} + m_5 + m_6 &= \frac{\tilde{F}_c}{\tilde{m}\tilde{l}} \{ \mathbf{n}_1^{\circ} \times (-\mu_+\mathbb{L}_{++}\delta_{++}^{\circ\perp} + \mu_-\mathbb{L}_{--}\delta_{--}^{\circ\perp} + \mu_+\mathbb{L}_{+-}\delta_{+-}^{\circ\perp} - \mu_-\mathbb{L}_{-+}\delta_{-+}^{\circ\perp}) \\ &\quad + \mathbf{n}_1^{\circ\perp} \times [\mu_+(\mathbf{F}_{+-}^{\circ} - \mathbf{F}_{++}^{\circ}) - \mu_-(\mathbf{F}_{-+}^{\circ} - \mathbf{F}_{--}^{\circ})] \} = 0. \end{aligned} \quad (\text{C16})$$

A similar argument shows that $\mathbf{m}_4 \cdot \delta^{\circ\perp} + m_6 + m_7 = 0$, which completes the proof.

2. Rotating modes

To assess the stability of rotating bound states, we use the results from Appendix C 1. Substituting the rotating base state solutions directly into Eq. (C8) would result in a system of equations with time-varying coefficients, so we first transform Eq. (C8) into a frame rotating with the orbital frequency ω_0 . To that end, we let $\hat{\mathbf{r}}_0 = (\cos \omega_0 t, \sin \omega_0 t)$ and $\hat{\boldsymbol{\theta}}_0 = (-\sin \omega_0 t, \cos \omega_0 t)$, and define the 2×2 matrix $\boldsymbol{\Omega} = (\hat{\mathbf{r}}_0 \quad \hat{\boldsymbol{\theta}}_0)$. Since $\frac{d}{dt}(\boldsymbol{\Omega}\mathbf{v}) = \dot{\boldsymbol{\Omega}}\mathbf{v} + \boldsymbol{\Omega}\dot{\mathbf{v}}$, we define the transformed vector $\tilde{\mathbf{z}}$ by $\mathcal{R}\tilde{\mathbf{z}} = \mathbf{z}$, where \mathcal{R} is the 10×10 matrix

$$\mathcal{R} = \begin{pmatrix} \boldsymbol{\Omega} & \mathbb{Z} & \mathbb{Z} & \mathbb{Z} & \mathbb{Z} \\ \mathbb{Z} & \boldsymbol{\Omega} & \mathbb{Z} & \mathbb{Z} & \mathbb{Z} \\ \dot{\boldsymbol{\Omega}} & \mathbb{Z} & \dot{\boldsymbol{\Omega}} & \mathbb{Z} & \mathbb{Z} \\ \mathbb{Z} & \mathbb{Z} & \mathbb{Z} & \mathbb{I} & \mathbb{Z} \\ \mathbb{Z} & \mathbb{Z} & \mathbb{Z} & \mathbb{Z} & \mathbb{I} \end{pmatrix}. \quad (\text{C17})$$

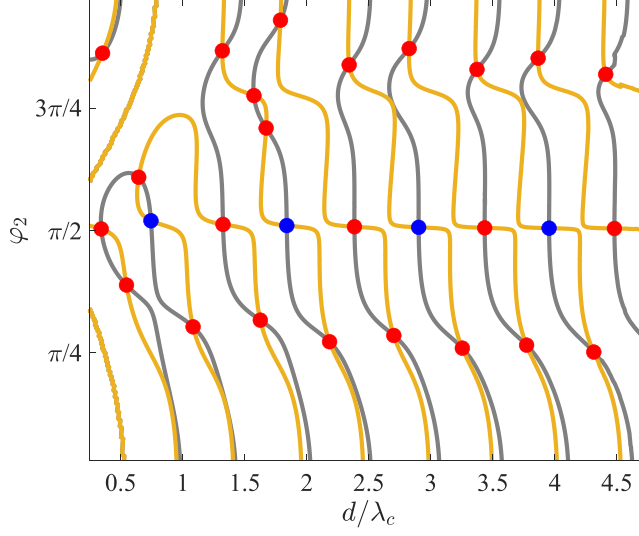


FIG. 12. Illustration of the numerical method used to locate promenade mode solutions, as described in Sec. VB. The curves are zero contours of the functions $F_P(d, \varphi_2)$ (gray) and $T_P(d, \varphi_2)$ (yellow), as defined in Eq. (36), where d is the distance between surfers and φ_2 the orientation angle. Equilibrium solutions are given by the intersections of the contours, with stable (unstable) points marked in blue (red). The parameters are given in Table I, with $\gamma = 3.3g$ and $f = 100$ Hz.

The linearized equations $\frac{d}{dt}\mathbf{z} = \mathcal{M}\mathbf{z}$ transform into $\frac{d}{dt}\tilde{\mathbf{z}} = \tilde{\mathcal{M}}\tilde{\mathbf{z}}$, where

$$\begin{aligned} \tilde{\mathcal{M}} &= \mathcal{R}^{-1}(\mathcal{M}\mathcal{R} - \dot{\mathcal{R}}) \\ &= \begin{pmatrix} \mathbb{Z} & \mathbb{Z} & \mathbb{I} & \mathbb{Z} & \mathbb{Z} \\ \mathbb{Z} & -\mathbb{I}/\tilde{m} + \omega_0\mathbb{J} & \mathbb{Z} & \boldsymbol{\Omega}^T\mathbb{N} & \mathbb{Z} \\ \omega_0^2\mathbb{I} + \boldsymbol{\Omega}^T\mathbb{F}_1\boldsymbol{\Omega} + \omega_0\mathbb{J}/\tilde{m} & \mathbb{Z} & 2\omega_0\mathbb{J} - \mathbb{I}/\tilde{m} & \boldsymbol{\Omega}^T\mathbb{F}_2 & \mathbb{Z} \\ \mathbb{Z} & \mathbb{Z} & \mathbb{Z} & \mathbb{Z} & \mathbb{I} \\ \mathbb{T}_1\boldsymbol{\Omega} & \mathbb{Z} & \mathbb{Z} & \mathbb{T}_2 & -\mathbb{I}/\tilde{m} \end{pmatrix} \quad (\text{C18}) \end{aligned}$$

and $\mathbb{J} = \begin{pmatrix} 0 & 1 \\ -1 & 0 \end{pmatrix}$. As with the rectilinear modes, the matrix $\tilde{\mathcal{M}}$ has a zero eigenvalue due to the invariance of the orbital solutions under rotation (Appendix C2a). The stability of the solutions is thus determined by the remaining eigenvalues; a solution is stable if all of the eigenvalues have negative real part, and is unstable otherwise.

a. Rotational invariance of rotating modes

Using arguments analogous to those in Appendix C1a, we show that

$$\mathbf{v} = \left(\boldsymbol{\Omega}^T\boldsymbol{\delta}^{\circ\perp} \quad -\left(\omega_0\mathbb{J} - \frac{1}{\tilde{m}}\mathbb{I}\right)^{-1}\boldsymbol{\Omega}^T\mathbb{N}\mathbf{1} \quad \mathbf{0} \quad \mathbf{1} \quad \mathbf{0} \right)^T \quad (\text{C19})$$

is in the nullspace of the matrix $\tilde{\mathcal{M}}$. The first, second, and fourth entries of the product $\tilde{\mathcal{M}}\mathbf{v}$ are identically zero. The third entry is

$$\begin{aligned} \left(\omega_0^2\mathbb{I} + \boldsymbol{\Omega}^T\mathbb{F}_1\boldsymbol{\Omega} + \frac{\omega_0\mathbb{J}}{\tilde{m}} \right) \boldsymbol{\Omega}^T\boldsymbol{\delta}^{\circ\perp} + \boldsymbol{\Omega}^T\mathbb{F}_2\mathbf{1} &= \boldsymbol{\Omega}^T \left[\left(\omega_0^2\mathbb{I} + \frac{\omega_0\mathbb{J}}{\tilde{m}} + \mathbb{F}_1 \right) \boldsymbol{\delta}^{\circ\perp} + \mathbb{F}_2\mathbf{1} \right] \\ &= \boldsymbol{\Omega}^T \left[\left(\omega_0^2\mathbb{I} + \frac{\omega_0\mathbb{J}}{\tilde{m}} + \mathbb{F}_1 \right) \boldsymbol{\delta}^{\circ\perp} + \mathbf{m}_1 + \mathbf{m}_2 \right]. \quad (\text{C20}) \end{aligned}$$

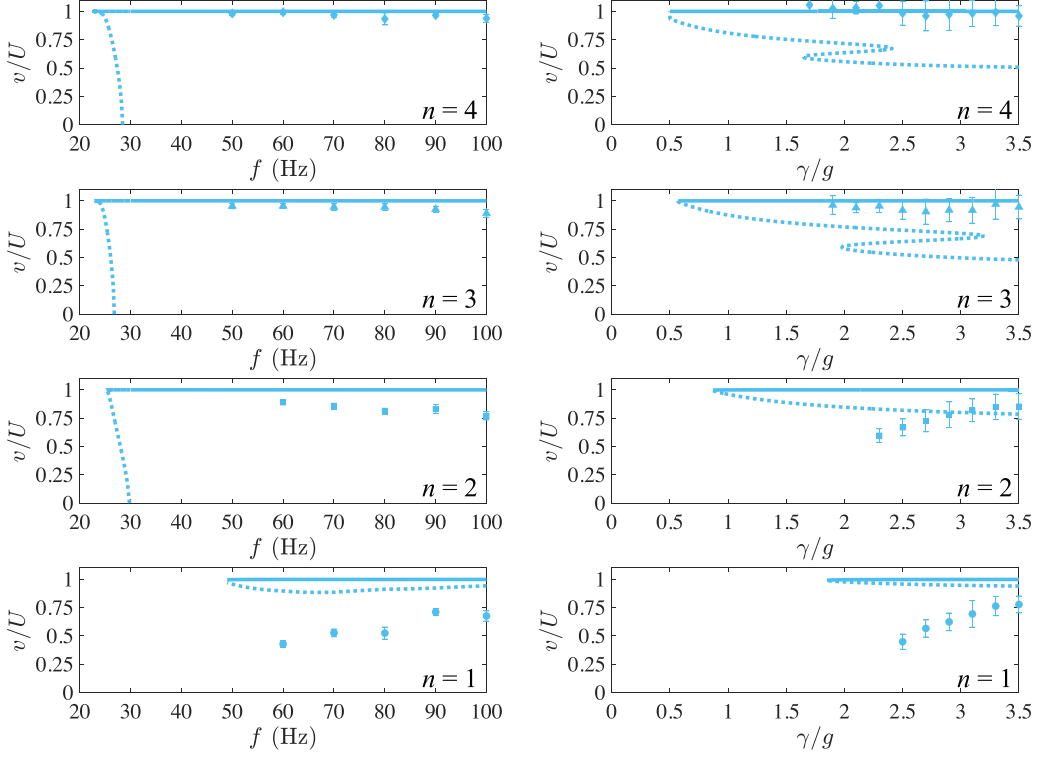


FIG. 13. Comparison between theory (curves) and experiment (points, [32]) for the surfers' speed v in the promenade mode, scaled by the free speed U . The left column shows the dependence of the speed on the forcing frequency f , where f and γ are varied together, as described in Sec. V A. The corresponding results for the distance between surfers are shown in Fig. 6. The right column shows the dependence of the speed on the forcing acceleration γ/g for the fixed forcing frequency $f = 100$ Hz; the corresponding results for the distance between surfers are shown in Fig. 7. Different rows are labeled by their corresponding mode orders n . Stable (unstable) modes are indicated by the solid (dashed) curves. For the sake of simplicity we show only the (cyan) solution branches in which stable promenade modes are found.

Using Eq. (C14), the term in the square brackets may be simplified to

$$\omega_0^2 \delta^{\circ\perp} + \frac{\omega_0}{\tilde{m}} \delta^{\circ} + \frac{n_2^{\circ\perp} - n_1^{\circ\perp}}{\tilde{m}} - \frac{2\tilde{F}_c}{\tilde{m}} [\mu_+^2 \mathbf{F}_{++}^{\circ\perp} + \mu_+ \mu_- (\mathbf{F}_{+-}^{\circ\perp} + \mathbf{F}_{-+}^{\circ\perp}) + \mu_-^2 \mathbf{F}_{--}^{\circ\perp}], \quad (\text{C21})$$

which is zero by Eq. (C1b). The fifth entry in $\tilde{M}\mathbf{v}$ is $\mathbb{T}_1 \delta^{\circ\perp} + \mathbb{T}_2 \mathbf{1}$, which is zero as shown in Appendix C 1 a.

APPENDIX D: SPEED OF SURFERS IN BOUND STATES

Figure 13 shows a comparison between theory and experiment for the surfers' speed in the promenade mode, across different values of forcing acceleration γ and forcing frequency f . Table II shows a comparison between theory and experiment for the surfers' speed in four of the bound states considered in the main text, for the single parameter combination $f = 100$ Hz and $\gamma/g = 3.3$.

TABLE II. Comparison between theory and experiment for the surfer speed in one of four bound states (tailgate, orbit, t-bone, and jackknife) and one of two orbit orders ($n = 1$ and $n = 2$). Numerical values are the dimensionless speed v/U , v being the surfer speed and U the free speed of an isolated surfer, for the parameter combination $f = 100$ Hz and $\gamma/g = 3.3$. The experimental values are given in Table S1 in Ref. [32], and blank entries indicate modes that were not measured in experiment. Note that in the t-bone and jackknife modes the two surfers have different speeds.

	Tailgate		Orbit		T-bone		Jackknife	
	Experiment	Theory	Experiment	Theory	Experiment	Theory	Experiment	Theory
$n = 1$	0.9 ± 0.1	1	1.1 ± 0.1	0.58	1.1 ± 0.1	0.95	1.5 ± 0.2	1.05
					0.4 ± 0.1	0.55	0.9 ± 0.1	0.52
$n = 2$		1	1.1 ± 0.1	0.89		1.04	1.2 ± 0.1	1.11
						0.54	0.8 ± 0.1	0.45

APPENDIX E: VIDEO CAPTIONS

Video 1: Left panel shows the weakly viscous gravity-capillary wave field (9) corresponding to a point particle oscillating at the origin with period $T = 1/f$. Right panel shows the inviscid capillary wave field derived in Eq. (A12). The scale bars denote the capillary wavelength λ_c . The parameters correspond to those given in Table I, with forcing frequency $f = 100$ Hz.

Video 2: First three tailgating modes and corresponding wave fields for $f = 100$ Hz and $\gamma/g = 3.3$, as shown in Fig. 5. The scale bars denote the capillary wavelength λ_c .

Video 3: First four promenade modes and corresponding wave fields for $f = 100$ Hz and $\gamma/g = 3.3$, as shown in Fig. 6. The scale bars denote the capillary wavelength λ_c .

Video 4: First four orbiting modes and corresponding wave fields for $f = 100$ Hz and $\gamma/g = 3.3$, as shown in Fig. 8. The scale bars denote the capillary wavelength λ_c .

Video 5: Top (bottom) row shows the first three t-bone (jackknife) modes and corresponding wave fields for $f = 100$ Hz and $\gamma/g = 3.3$, as shown in Fig. 9. The scale bars denote the capillary wavelength λ_c .

Video 6: A four-surfer promenade mode and corresponding wave field for $f = 100$ Hz and $\gamma/g = 3.3$, as shown in Fig. 10(a). Neighbors are separated by approximately one capillary wavelength λ_c , which is indicated by the scale bar.

Video 7: An eight-surfer super-orbiting mode and corresponding wave field for $f = 100$ Hz and $\gamma/g = 3.3$, as shown in Fig. 10(b). The scale bars denote the capillary wavelength λ_c .

Video 8: A flocking state of 13 surfers and corresponding wave field for $f = 100$ Hz and $\gamma/g = 3.3$, as shown in Fig. 10(c). Pairs of surfers are separated by approximately one or two capillary wavelengths λ_c , which is indicated by the scale bar.

Video 9: A flocking state of 16 surfers and corresponding wave field for $f = 100$ Hz and $\gamma/g = 3.3$, as shown in Fig. 10(d). Neighboring surfers are separated in both the horizontal and vertical directions by approximately three capillary wavelengths λ_c , which is indicated by the scale bar.

-
- [1] M. C. Marchetti, J. F. Joanny, S. Ramaswamy, T. B. Liverpool, J. Prost, M. Rao, and R. A. Simha, Hydrodynamics of soft active matter, *Rev. Mod. Phys.* **85**, 1143 (2013).
 - [2] S. Ramaswamy, The mechanics and statistics of active matter, *Annu. Rev. Condens. Matter Phys.* **1**, 323 (2010).
 - [3] G. Gompper, R. G. Winkler, T. Speck, A. Solon, C. Nardini, F. Peruani, H. Löwen, R. Golestanian, U. B. Kaupp, L. Alvarez *et al.*, The 2020 motile active matter roadmap, *J. Phys.: Condens. Matter* **32**, 193001 (2020).

- [4] R. G. Winkler and G. Gompper, Hydrodynamics in motile active matter, in *Handbook of Materials Modeling, Methods: Theory and Modeling*, edited by W. Andreoni and S. Yip (Springer, Cham, 2020), pp. 1471–1491.
- [5] C. Dombrowski, L. Cisneros, S. Chatkaew, R. E. Goldstein, and J. O. Kessler, Self-concentration and large-scale coherence in bacterial dynamics, *Phys. Rev. Lett.* **93**, 098103 (2004).
- [6] H. H. Wensink, J. Dunkel, S. Heidenreich, K. Drescher, R. E. Goldstein, H. Löwen, and J. M. Yeomans, Meso-scale turbulence in living fluids, *Proc. Natl. Acad. Sci. USA* **109**, 14308 (2012).
- [7] S. Portugal, T. Hubel, J. Fritz, S. Heese, D. Trobe, B. Voelkl, S. Hailes, A. M. Wilson, and J. R. Usherwood, Upwash exploitation and downwash avoidance by flap phasing in ibis formation flight, *Nature (London)* **505**, 399 (2014).
- [8] I. Ashraf, H. Bradshaw, T.-T. Ha, J. Halloy, R. Godoy-Diana, and B. Thiria, Simple phalanx pattern leads to energy saving in cohesive fish schooling, *Proc. Natl. Acad. Sci. USA* **114**, 9599 (2017).
- [9] T. Y. Wu, Fish swimming and bird/insect flight, *Annu. Rev. Fluid Mech.* **43**, 25 (2011).
- [10] D. Klotz, As above, so below, and also in between: Mesoscale active matter in fluids, *Soft Matter* **15**, 8946 (2019).
- [11] S. T. Hsieh and G. V. Lauder, Running on water: Three-dimensional force generation by basilisk lizards, *Proc. Natl. Acad. Sci. USA* **101**, 16784 (2004).
- [12] J. W. M. Bush and D. L. Hu, Walking on water: Bioloocomotion at the interface, *Annu. Rev. Fluid Mech.* **38**, 339 (2006).
- [13] D. L. Hu, B. Chan, and J. W. M. Bush, The hydrodynamics of water strider locomotion, *Nature (London)* **424**, 663 (2003).
- [14] D. L. Hu and J. W. M. Bush, Meniscus-climbing insects, *Nature (London)* **437**, 733 (2005).
- [15] J. Yuan and S. K. Cho, Bio-inspired micro/mini propulsion at air-water interface: A review, *J. Mech. Sci. Tech.* **26**, 3761 (2012).
- [16] A. Snezhko, M. Belkin, I. S. Aranson, and W.-K. Kwok, Self-assembled magnetic surface swimmers, *Phys. Rev. Lett.* **102**, 118103 (2009).
- [17] G. Grosjean, G. Lagubeau, A. Darras, M. Hubert, G. Lumay, and N. Vandewalle, Remote control of self-assembled microswimmers, *Sci. Rep.* **5**, 16035 (2015).
- [18] G. Kokot, G. V. Kolmakov, I. S. Aranson, and A. Snezhko, Dynamic self-assembly and self-organized transport of magnetic micro-swimmers, *Sci. Rep.* **7**, 14726 (2017).
- [19] A. Sukhov, S. Ziegler, Q. Xie, O. Trosman, J. Pande, G. Grosjean, M. Hubert, N. Vandewalle, A.-S. Smith, and H. Jens, Optimal motion of triangular magnetocapillary swimmers, *J. Chem. Phys.* **151**, 124707 (2019).
- [20] J. Yuan and S. K. Cho, Mechanism and flow measurement of AC electrowetting propulsion on free surface, *Exp. Fluids* **56**, 67 (2015).
- [21] G. Pucci, E. Fort, M. Ben Amar, and Y. Couder, Mutual adaptation of a Faraday instability pattern with its flexible boundaries in floating fluid drops, *Phys. Rev. Lett.* **106**, 024503 (2011).
- [22] H. Ebata and M. Sano, Swimming droplets driven by a surface wave, *Sci. Rep.* **5**, 8546 (2015).
- [23] G. Pucci, Faraday instability in floating drops out of equilibrium: Motion and self-propulsion from wave radiation stress, *Int. J. Non Linear Mech.* **75**, 107 (2015).
- [24] Y. Couder, S. Protière, E. Fort, and A. Boudaoud, Walking and orbiting droplets, *Nature (London)* **437**, 208 (2005).
- [25] J. W. M. Bush and A. U. Oza, Hydrodynamic quantum analogs, *Rep. Prog. Phys.* **84**, 017001 (2021).
- [26] M. Nagayama, S. Nakata, Y. Doi, and Y. Hayashima, A theoretical and experimental study on the unidirectional motion of a camphor disk, *Physica D* **194**, 151 (2004).
- [27] Y. Hirose, Y. Yasugahira, M. Okamoto, Y. Koyano, H. Kitahata, M. Nagayama, and Y. Sumino, Two floating camphor particles interacting through the lateral capillary force, *J. Phys. Soc. Jpn.* **89**, 074004 (2020).
- [28] M. I. Kohira, Y. Hayashima, M. Nagayama, and S. Nakata, Synchronized self-motion of two camphor boats, *Langmuir* **17**, 7124 (2001).
- [29] N. J. Suematsu, S. Nakata, A. Awazu, and H. Nishimori, Collective behavior of inanimate boats, *Phys. Rev. E* **81**, 056210 (2010).

- [30] E. Heisler, N. J. Suematsu, A. Awazu, and H. Nishimori, Swarming of self-propelled camphor boats, [*Phys. Rev. E* **85**, 055201\(R\) \(2012\)](#).
- [31] Y. S. Ikura, E. Heisler, A. Awazu, H. Nishimori, and S. Nakata, Collective motion of symmetric camphor papers in an annular water channel, [*Phys. Rev. E* **88**, 012911 \(2013\)](#).
- [32] I. Ho, G. Pucci, A. U. Oza, and D. M. Harris, preceding paper, Capillary surfers: Wave-driven particles at a vibrating fluid interface, [*Phys. Rev. Fluids* **8**, L112001 \(2023\)](#).
- [33] M. Faraday, On a peculiar class of acoustical figures; and on certain forms assumed by groups of particles upon vibrating elastic surfaces, [*Philos. Trans. R. Soc. London* **121**, 299 \(1831\)](#).
- [34] D. Y. C. Chan, J. D. Henry, Jr., and L. R. White, The interaction of colloidal particles collected at fluid interfaces, [*J. Colloid Interface Sci.* **79**, 410 \(1981\)](#).
- [35] P. Kralchevsky, V. Paunov, I. Ivanov, and K. Nagayama, Capillary meniscus interaction between colloidal particles attached to a liquid–fluid interface, [*J. Colloid Interface Sci.* **151**, 79 \(1992\)](#).
- [36] D. Vella and L. Mahadevan, The “Cheerios” effect, [*Am. J. Phys.* **73**, 817 \(2005\)](#).
- [37] M. Oettel, A. Domínguez, and S. Dietrich, Effective capillary interaction of spherical particles at fluid interfaces, [*Phys. Rev. E* **71**, 051401 \(2005\)](#).
- [38] K. D. Danov, P. A. Kralchevsky, B. N. Naydenov, and G. Brenn, Interactions between particles with an undulated contact line at a fluid interface: Capillary multipoles of arbitrary order, [*J. Colloid Interface Sci.* **287**, 121 \(2005\)](#).
- [39] P. A. Kralchevsky and K. Nagayama, Capillary interactions between particles bound to interfaces, liquid films and biomembranes, [*Adv. Colloid Interface Sci.* **85**, 145 \(2000\)](#).
- [40] M. Oettel and S. Dietrich, Colloidal interactions at fluid interfaces, [*Langmuir* **24**, 1425 \(2008\)](#).
- [41] F. John, On the motion of floating bodies II. Simple harmonic motions, [*Commun. Pure Appl. Math.* **3**, 45 \(1950\)](#).
- [42] F. Ursell, On the heaving motion of a circular cylinder on the surface of a fluid, [*Q. J. Mech. Appl. Math.* **2**, 218 \(1949\)](#).
- [43] F. Ursell and G. I. Taylor, Short surface waves due to an oscillating immersed body, [*Proc. R. Soc. London A* **220**, 90 \(1953\)](#).
- [44] F. G. Leppington, On the radiation and scattering of short surface waves. Part 1, [*J. Fluid Mech.* **56**, 101 \(1972\)](#).
- [45] F. G. Leppington, On the radiation and scattering of short surface waves. Part 2, [*J. Fluid Mech.* **59**, 129 \(1973\)](#).
- [46] P. F. Rhodes-Robinson and F. J. Ursell, On the short surface waves due to a half-immersed circular cylinder oscillating on water of infinite depth, [*Proc. R. Soc. London A* **384**, 333 \(1982\)](#).
- [47] M. J. Simon and F. J. Ursell, The high-frequency radiation of water waves by oscillating bodies, [*Proc. R. Soc. London A* **401**, 89 \(1985\)](#).
- [48] J. B. Keller, Water wave production by oscillating bodies, [*IMA J. Appl. Math.* **78**, 839 \(2013\)](#).
- [49] M. De Corato and V. Garbin, Capillary interactions between dynamically forced particles adsorbed at a planar interface and on a bubble, [*J. Fluid Mech.* **847**, 71 \(2018\)](#).
- [50] H. Lamb, *Hydrodynamics* (Cambridge University Press, Cambridge, 1932).
- [51] F. Dias, A. Dyachenko, and V. E. Zakharov, Theory of weakly damped free-surface flows: A new formulation based on potential flow solutions, [*Phys. Lett. A* **372**, 1297 \(2008\)](#).
- [52] P. Milewski, C. Galeano-Rios, A. Nachbin, and J. W. M. Bush, Faraday pilot-wave dynamics: Modelling and computation, [*J. Fluid Mech.* **778**, 361 \(2015\)](#).
- [53] M. Durey and P. A. Milewski, Faraday wave-droplet dynamics: Discrete-time analysis, [*J. Fluid Mech.* **821**, 296 \(2017\)](#).
- [54] C. A. Galeano-Rios, M. M. P. Couchman, P. Caldarou, and J. W. M. Bush, Ratcheting droplet pairs, [*Chaos* **28**, 096112 \(2018\)](#).
- [55] C. A. Galeano-Rios, P. A. Milewski, and J.-M. Vanden-Broeck, Quasi-normal free-surface impacts, capillary rebounds and application to Faraday walkers, [*J. Fluid Mech.* **873**, 856 \(2019\)](#).
- [56] A. Nachbin, P. A. Milewski, and J. W. M. Bush, Tunneling with a hydrodynamic pilot-wave model, [*Phys. Rev. Fluids* **2**, 034801 \(2017\)](#).

- [57] M. Durey, P. A. Milewski, and Z. Wang, Faraday pilot-wave dynamics in a circular corral, *J. Fluid Mech.* **891**, A3 (2020).
- [58] C. A. Galeano-Rios, R. Cimpanu, I. A. Bauman, A. MacEwen, P. A. Milewski, and D. M. Harris, Capillary-scale solid rebounds: Experiments, modelling and simulations, *J. Fluid Mech.* **912**, A17 (2021).
- [59] L. F. Alventosa, R. Cimpanu, and D. M. Harris, Inertio-capillary rebound of a droplet impacting a fluid bath, *J. Fluid Mech.* **958**, A24 (2023).
- [60] M. Abramowitz and I. A. Stegun, *Handbook of Mathematical Functions with Formulas, Graphs, and Mathematical Tables*, edited by National Bureau of Standards, United States Department of Commerce, Vol. 55 (Martino Publishing, Mansfield, CT, 2014).
- [61] A. Domínguez, M. Oettel, and S. Dietrich, Force balance of particles trapped at fluid interfaces, *J. Chem. Phys.* **128**, 114904 (2008).
- [62] G. Pucci, I. Ho, and D. M. Harris, Friction on water sliders, *Sci. Rep.* **9**, 4095 (2019).
- [63] T. P. Theodoulidis, Struve functions, MATLAB Central File Exchange, <https://www.mathworks.com/matlabcentral/fileexchange/37302-struve-functions> (2020).
- [64] D. Schwarz, Fast and robust curve intersections, MATLAB Central File Exchange, version 1.12, <https://www.mathworks.com/matlabcentral/fileexchange/11837-fast-and-robust-curve-intersections> (2015).
- [65] J. Arbelaiz, A. U. Oza, and J. W. M. Bush, Promenading pairs of walking droplets: Dynamics and stability, *Phys. Rev. Fluids* **3**, 013604 (2018).
- [66] A. U. Oza, E. Siéfert, D. M. Harris, J. Moláček, and J. W. M. Bush, Orbiting pairs of walking droplets: Dynamics and stability, *Phys. Rev. Fluids* **2**, 053601 (2017).
- [67] A. He, K. Nguyen, and S. Mandre, Capillary interactions between nearby interfacial objects, *Europhys. Lett.* **102**, 38001 (2013).
- [68] A. P. Prudnikov, Y. A. Brychkov, O. I. Marichev, and R. H. Romer, *Integrals and Series, Vol. 2: Special Functions* (Gordon and Breach, New York, 1992), Chap. 2.12.3.6, p. 175.
- [69] F. W. J. Olver, A. B. Olde Daalhuis, D. W. Lozier, B. I. Schneider, R. F. Boisvert, C. W. Clark, B. R. Miller, B. V. Saunders, H. S. Cohl, and M. A. McClain (eds.), NIST Digital Library of Mathematical Functions, release 1.1.5, <http://dlmf.nist.gov/> (2022), Eq. 10.11.6, Eq. 11.6.1, Eq. 10.17.6.